Full-scale measurements of slamming loads and responses on high-speed planing craft in waves

J. Camilleri[a,*], D. J. Taunton[a] & P. Temarel[a]

[a] Fluid Structure Interactions Group, Faculty of Engineering and the Environment, University of Southampton, Southampton SO16 7QF, UK

Abstract

Full-scale trials on a high-speed planing craft in waves were conducted to investigate the characteristics of slamming impacts and related rigid body and structural response. Measurements of acceleration, pressure, strain and global hull deflection were made in different sea conditions and at different speeds and headings. Low pass filtering is used to remove unwanted noise from the acceleration signals and extract the rigid body response. Methods for removing trends from the strain signals and identifying the peaks in the pressure and strain signals are established. Characteristic results including time series, distributions of peak values, averages of the largest 1/3rd and 1/10th peak values and individual impact events, are presented and discussed. The Weibull and Generalized Pareto models are used to describe the pressure and strain peak values and for estimating extreme loads and responses. Automated algorithms for fitting the statistical models to the peak value distributions are developed and the goodness-of-fit of the models to the data is examined.

Keywords: slamming; planing craft; experiments; data processing; statistical analysis

1. Introduction

Planing craft travelling at high-speed in waves frequently experience severe slamming impacts. The nonlinear nature of high-speed craft motions and randomness of the wave environment implies that each hull-water impact is unique. The characteristics of the resulting impact loads, which act on the hull bottom, depend on a number of parameters. The most important in terms of severity of impact are the trim angle, hull deadrise angle and impact velocity at the instant of impact with water (Allen & Jones 1978). The response of high-speed planing craft to slamming impacts is mainly characterised by transient and dynamic accelerations and local structural deformations. Slamming impacts can thus have an adverse effect on the hull structure, human comfort and performance, and equipment.

The importance of slamming impact loads for high-speed planing craft has led to a significant body of work trying to understand the complex physics involved and model the impacts using a wide range of methods, see for example Temarel et al. (2016). The interest in the present work lies in experimental studies, both full-scale and model-scale investigations, and the methods used to analyse the data. Full-scale trials are expensive to conduct and usually confidential to the ship builder or owner. Full-scale data for loads and responses on high-speed planing craft in waves is therefore not widely available.

One of the early and most significant works is that of Allen & Jones (1978) who measured pressure, acceleration and strain on two planing hulls in waves. The measured data together with the results from a semi-empirical method were used to develop a simplified method for predicting the hull bottom impact pressure loads for structural design purposes that is still widely used today. Garme & Rosén (2003) conducted full-scale trials on a high-speed planing craft in waves to study the characteristics of slamming impacts and gather data for validating their numerical model. The craft was a Storebro 90E and has an overall length of 9.5 m, displacement of 6.5 tonnes, deadrise angle at amidships of 22° and a maximum speed of +40 knots. Measurements of rigid body motions and accelerations, pressures and laminate and shear strain were made in different sea conditions (significant wave heights ranging from 0.4 m to 1.5 m and mean periods from 2.5 s to 4 s), and at different speeds

---

* Corresponding author.
E-mail address: jc1d13@soton.ac.uk, j.camilleri91@gmail.com

(ranging from 10 to 40 knots) and headings (head and bow seas). The impact pressures recorded in bow seas (the angle between boat and wave direction μ = 150°) were found to be significantly higher than in head seas (μ = 180°), which are generally considered as the most severe condition regarding impact loads because here the largest relative motions and velocities are experienced. This was concluded to be due to smaller effective deadrise angle, i.e. the relative angle between the hull and water surface at the moment of impact, in bow seas. The vertical accelerations recorded in bow seas were, however, lower than head seas, which is attributed to the fact that in bow seas the high pressure loading acts on a smaller area of the hull, thus resulting in lower forces and accelerations. The semi-empirical methods used in the design of high-speed craft assume direct relationship between rigid body accelerations and pressure and, thus, may underestimate the loading in such conditions. The statistical averages of the peak pressures and structural responses were also found to correlate well. Mørch & Hermundstad (2005) measured accelerations, pressures, strains, and local panel deflections on a high-speed recreational craft to understand better the impact loads experienced in waves for design purposes. The craft (Nidelv 610) has an overall length of 6.1 m, fully loaded displacement of 1870 kg, deadrise angle of 19.5° and a top speed of 40 knots. Tests were performed in different sea states (significant wave heights ranging from 0.32 m to 0.55 m) at various speeds (ranging from 30 to 40 knots) and headings in both fully and partially loaded conditions. The loads and responses measured in the fully loaded condition were found to be lower than those measured in the partially loaded condition (displacement of 1550 kg). From comparisons of the pressure and strain measurements with the DNV (1997) rules it is found that design pressures are too low and that there is a large safety margin for the required laminate thickness based on design pressures. Riley et al. (2014) performed a detailed investigation into the characteristics of accelerations measured on high-speed craft in waves and presented a method quantifying wave impacts loads using full-scale acceleration data, in particular the amplitude and duration of rigid body heave acceleration. The acceleration data recorded during the seakeeping trials of a large number of manned and unmanned high-speed planing craft in moderate and rough seas was used. The crafts tested have lengths ranging from 10 to 25 m and displacements ranging from approximately 6.35 to 52.6 tonnes. Significant wave heights varied from approximately 0.6 to 2 m and forward speeds varied from 8 to 45 knots.

Model scale investigations of loads and responses on high-speed planing craft include both free-fall or constant velocity water impact tests, e.g. Tveitnes et al. (2008), Lewis et al. (2010) and Allen & Battley (2015), and towing tank tests in waves, e.g. Fridsma (1971), Rosén & Garme (2004), Taunton et al. (2011), Begovic et al. (2014) and Judge et al. (2015). In water impact tests a common approach is to simplify the complex three-dimensional hull water impact problem to a transverse section, e.g. a wedge or even a hull panel, vertically impacting the calm water surface. Impact tests provide useful insight into the physics of slamming and the effect of several parameters on the loads and responses; however, there is no consensus as to whether the loads and responses measured on a wedge accurately reflect those measured on a full-scale craft. Towing tank tests are a better representation of the full-scale problem. Rosén & Garme (2004) performed a detailed investigation into the pressure distribution on planing craft in waves. The model hull is a simplified version of the full-scale craft tested by Garme & Rosén (2003) with a scale of 1:10. The model was tested in calm water, and regular and irregular head and oblique waves at three speeds. The measurements made include rigid body motions and acceleration and pressures. A dense matrix of pressure sensors and high sampling frequency (2.5 kHz) was used to accurately capture the transient and highly localized pressure distribution. The sampling frequency was found to be sufficient in most cases except for extreme impacts where the rise times are of the order of 1ms. A method for reconstructing the complete pressure distribution on the hull surface from the discrete point measurements is presented. The impact loads obtained from integrating the reconstructed pressure distribution are found to correlate relatively well with the inertia force derived from the acceleration signal. It is concluded that observed differences are due to the fact that the derived pressure force only considers the load acting on the forward part of the hull (the instrumented area), whereas the acceleration-derived force is related to the total load on the hull. Begovic et al. (2014) investigated the influence of bottom warping, i.e. deadrise angle variation along the hull length, on the seakeeping performance of planing hulls using model tests. One monohedral (β = 16.7°) and three warped (deadrise angle varies linearly from transom to 0.8L) hard chine planing hull forms were tested in regular waves at three speeds (C_V = 0.942, 1.275 and 1.594). The choice of regular waves was to provide a database for numerical model validation and obtain better insight into the physics of the responses. Model speed, heave, pitch, added resistance and accelerations at the bow and close to midship were measured during the tests. Bottom warping is found to have limited effect on the motions but significant effect on the bow accelerations, particularly at high speed where lower accelerations were measured on more warped hulls. Spectral analysis of the data further revealed that bottom warping has a larger influence on higher order acceleration harmonics than the first harmonic. Taunton et al. (2011) developed a new series of high-speed hard chine planing hulls and performed an extensive investigation into their motions and accelerations in waves. The series has L/B ratios typical of modern high-speed interceptor craft and race boats and a deadrise angle of 22.5°. The models were tested in irregular head waves at three speeds. The Cartwright & Longuet-Higgins and Gamma distributions were fitted to heave and pitch motions and accelerations respectively. A method for predicting human performance on-board full-scale craft using the statistical data is presented.

The lack of full-scale experimental studies in the literature is also partly due to the complexities involved in making full-scale measurements and processing the data. Two common issues related to making measurements on high-speed planing craft in waves are noise in the acceleration signals, and identification of peaks. Data measured on high-speed planing craft in waves, in particular acceleration data, often contains unwanted high-frequency noise that is caused by structural vibrations and engine and propeller vibrations in full-scale tests and by test model and towing carriage vibrations in model tests (Savitsky, 2016). Low pass filtering is commonly used to extract the rigid body response from the noisy signal, see for example Rosén & Garme (2004), Riley et al. (2014) and Savitsky (2016). Riley et al. (2014) concluded from the analysis of a large number of signals that a cut-off frequency of 10Hz effectively removes the high-frequency vibration content without significantly affecting the rigid body response. Savitsky (2016) showed that the frequency content of individual hull-wave impact accelerations is a function of the impact velocity, deadrise angle and craft weight. The cut-off frequency, thus, needs to be chosen carefully.

Peak values are often used for characterization of slamming impacts, for example the average of largest 1/10th pressure or strain peaks, and for estimating extreme loads or responses. Accurate identification of the peaks is, therefore, important however challenging. Allen et al. (2008) presented an algorithm for identifying peaks in acceleration signals recorded on an Atlantic 75 RIB. The algorithm uses the signal characteristics, in particular the high rate of change of acceleration associated with impact, to identify the timing of events from which the peak magnitude and changes in boat motion, i.e., pitch, roll and yaw, following impact are determined. Jacobi et al. (2014) used a rate of change of stress criterion together with the pitch motion signal to accurately identify the peaks in stress signals recorded on a 98 m wave piercer catamaran. In their algorithm a slam event is defined as one where (1) the rate of change of stress exceeds the product of a specified constant and the yield stress of the material and (2) the pitch is positive indicating bow down motion. The second criterion is used because the whipping after a slam event was also found to have a high rate of change of stress which resulted in many whipping events being incorrectly identified as slam events. The peak is then the maximum stress in the identified slam event. Riley et al. (2014) used two criteria to identify valid acceleration peaks – a vertical threshold equal to the Root Mean Square (RMS) of the signal and a horizontal threshold (sliding time window) calculated from the wave encounter frequency.

The behaviour of a high-speed planing craft in waves is strongly nonlinear and statistical methods are commonly used for characterization of the loads and responses and for extreme value prediction. Methods for calculating extreme loads and responses are well established (e.g. Ochi 1981) and involve fitting of analytical distribution functions to samples of observed or computed data and extrapolating for extreme values. Garme & Rosén (2003) fitted a two-parameter Weibull distribution to the measured pressure peaks. The peaks were found to belong to two different statistical distributions, namely the low magnitude peaks resulting from linear hull-wave interaction were found to follow a Rayleigh distribution whilst the large slamming induced peaks are approximately exponentially distributed. McCue (2012) studied the suitability of several statistical distributions to describe high-speed craft peak acceleration data. The distributions considered are the exponential, Rayleigh, lognormal, Gumbel, Weibull, Fréchet and Generalized Extreme Value (GEV). The exponential distribution suggested by Fridsma (1971), which is often used to estimate design loads, was consistently the worst fit to the data whilst GEV typically provided the best fit. The exponential distribution was found to be too conservative, adding that 'extra' factor of safety into the structural design process. Begovic et al. (2016) also investigated the suitability of a number of distributions to describe planing motions (normal, extreme value and Cartwright) and vertical bow and CG accelerations (exponential, Gamma and Weibull) using data from model tests on a monohedral prismatic hull and a warped hull in irregular head seas at four speeds. The results further confirm that planing hull motions are best described using a Cartwright distribution and that the exponential distribution is not a good fit to the acceleration data. The Weibull and Gamma distributions are found to perform equally well in terms of goodness-of-fit; however, the authors recommend the use of the former because of its simpler form.

The accuracy of extreme value estimates depends strongly on how well the statistical model fits the data, particularly in the tail of the distribution. The Peak-Over-Threshold (POT) method fits a distribution to the peaks above a threshold, thus improving the modelling of the largest peaks, hence the extreme value estimates. The POT method is based on Pickands (1975) theorem, which states that, for a large class of underlying distribution functions and large threshold, the distribution of the excesses is well approximated by the Generalized Pareto distribution (GPD). The POT method has been widely used for estimation of extreme wave loads on large ships (e.g. Wang & Moan (2004) and Wu & Moan (2006)), sloshing loads (e.g. Graczyk & Moan (2008)) and, more recently, high-speed craft accelerations Razola et al. (2016). Razola et al. (2016) studied in detail the statistical character of high-speed craft accelerations. The Weibull and Generalized Pareto distributions are used to describe the acceleration peaks and estimate extreme values. The Weibull model is only fitted to a fraction of the largest peak values to improve the accuracy of the extreme value estimates and an automated threshold selection algorithm is developed to reduce the subjectivity in selecting the threshold. An automated algorithm for selecting the GPD threshold based on the shape parameter stability plots is also presented. Both models fit the data well and predict similar most probable largest values. The extreme values with 1% probability of exceedance show, however, less agreement even for such large samples used, highlighting the challenges involved in predicting extreme events with low probability of occurrence.

There are many different approaches available for calculating the behaviour of high-speed planing craft in waves including, strip methods, panel methods (e.g. Boundary Element or Rankine Methods) or even Computational Fluid Dynamics. In strip methods, the complex 3D problem of a planing craft travelling at high speed in waves is simplified to the sum of a series of 2D sections or strips vertically impacting the clam water surface. Due to the nonlinear nature of the motions and loads, the equations of motion are solved in time domain to obtain the global response. Strip methods are therefore relatively efficient and practical for the early stages of design. Theoretical investigations of planing craft in waves using strip methods include the original work of Zarnick (1979) and more recently Keuning (1994), Akers (1999), Blake & Wilson (2001), Garme & Rosén (2003) and Garme (2005). The 2D water entry problem has also been widely studied starting with the pioneering works of von Karman (1929) who applied momentum theory to estimate the forces acting on seaplane floats during landing and Wagner (1932) who extended the von Karman (1929) model to account for the water pile-up at the intersection between the body and water surfaces. In the following years, several researchers attempted to improve the Wagner (1932) model and extensive reviews of these developments can be found in Faltinsen et al. (2004) and Korobkin (2004). The 2D water entry problem has also been studied using other methods including BEM (e.g. Zhao et al. 1996) and CFD (e.g. Stenius et al. 2011, Piro & Maki 2013).

The structural design of high-speed planing craft, particularly craft of length less than 20m, is largely governed by the slamming impact loads. Many designers of high-speed craft today still rely on past experience and semi-empirical methods (e.g. Savitsky & Brown, 1976; Allen & Jones, 1978) for the prediction of design loads. In these semi-empirical methods, which are also implemented in the design rules of several classification societies (e.g. DNV GL, 2015; Lloyd's Register 2016) and the ISO (2008) standard for small craft hull construction and scantlings, a design pressure load is calculated for each hull structural component (e.g. plating, stiffeners etc.) for stress analysis and scantling determination. Each component is analysed individually until the entire grillage is examined. These methods are simple and easy to use and require minimal input, which is important in the early design stages; however, they involve several simplifications. For instance, the highly dynamic and non-uniform slamming loads are treated as uniformly distributed static loads, and hydroelastic effects are not considered. Such simplifications may result in structural damage or heavy and inefficient structures.

Full-scale trials on a 9.6m high-speed planing craft in waves have been performed with the aim to gain further insight into the characteristics of slamming impacts and related global and local responses. An extensive set of data consisting of accelerations at the bow and near the LCG, pressure and strain at various locations across the hull bottom surface and global hull deflections in different sea conditions and at different forward speeds and headings was recorded. As is the case with the referenced works, the hydrodynamic impact pressure is measured with a matrix of pressure sensors of small diaphragm area. In the present study, four head sea runs covering a good range of sea and operational conditions are considered with the aim to illustrate the data processing procedure and present and discuss characteristic findings. Methods for processing the experimental data, including, low pass filtering the acceleration signals to remove the high frequency noise, removing the time varying offsets from the strain signals and identifying the peaks in the pressure and strain signals are described in detail with examples. Characteristic segments of the time signals and histograms of the peak values are presented and highlight the stochastic nature of the problem. The number of peaks identified in each signal together with the calculated averages of the largest 1/3rd and 1/10th peak values are used to assess the symmetry of impacts, variation of loads and responses across the hull bottom and the effect of forward speed and sea conditions. The characteristics of a typical impact event are also discussed. Statistical analysis of the measured data is also performed. The Weibull and Generalized Pareto models are fitted to the samples of pressure and strain peaks for estimating extreme values. Automated algorithms for fitting the statistical models to the peak value distributions are developed and the goodness-of-fit of the models to the data is examined. Finally, the relevance of this work to high-speed craft design is addressed by comparing the measurements with the predictions based on the rules of two Classification Societies, DNV GL (2015) and Lloyd's Register (2016), and the ISO 12215 standard (ISO, 2008).

2. Test description

2.1. Test craft

The C-Target 9 is a high-speed marine target used for naval gunnery training, weapons testing, and ship command and control assessments. It is designed and built by Autonomous Surface Vehicles (ASV) Ltd. The craft is shown in Figure 1 and the principal particulars are given in Table 1. The hull form is characterised by v-shaped sections and hard chines. Spray rails are also fitted. The lightweight aluminium craft is powered by two Mercury Verado 300HP outboards and can reach a speed of up to 50 knots (ASV 2017). At top speed, the Froude number (based on waterline length) $Fr_L = V/\sqrt{gL} = 3$ and the speed coefficient (based on transom beam) $C_V = V/\sqrt{gB} = 5.6$.

Figure 1 – C-Target 9 (ASV 2017).

Table 1 – Principal particulars of the C-Target 9 (ASV 2017).

Length overall, L_{OA}	9.6 m
Waterline length, L_{WL}	7.2 m
Waterline beam, B_{WL}	2.1 m
Draft, T	0.4 m
Deadrise angle, $\beta_{amidships}$	25.5 °
Displacement, Δ	≈2750 kg
LCG	2.4 m
VCG	0.72 m
Pitch radius of gyration, r_y	25.9% L_{WL}

2.2. Measurements and instrumentation

Measurements of accelerations, pressure, strain and global hull deflections were made during the trials. The layout of the sensors is shown in Figure 2. The longitudinal and transverse positions of the pressure sensors and strain gauges and deadrise angles of the instrumented transverse sections are given in Table 2.

The speed, position and heading of the craft were measured using the GPS plotter (GARMIN GPSmap 750s) installed on-board sampled at a rate of at 1Hz. The plotter was also used to mark the waypoints (route) to improve the repeatability of the tests. The accelerations were measured using tri-axial accelerometers at the bow and in the cockpit behind the seats (close to the craft's LCG). The bow accelerometer (Crossbow CXL100HF3, Range ±100g, Frequency 0.3 – 10,000 Hz) was bolted to the underside of the deck in the anchor hatch and the cockpit accelerometer (CFX USCA-TX, Range ±10g, Frequency DC – 200 Hz) was glued and strapped to the cockpit floor.

The impact loads were measured with a matrix of ICP® (Integrated Circuit Piezoelectric) pressure sensors positioned in a three-row grid pattern symmetric about the keel line as shown in Figure 2. The longitudinal position of the sensors was chosen based on the results of numerical simulations. The time-domain simulation model of Blake & Wilson (2001) was used to predict the vertical response of the craft in waves for a range of forward speeds, significant wave heights and zero crossing periods. The mean dynamic sinkage and trim were then calculated to identify which transverse hull sections are more likely to experience the largest number of slamming impacts. In addition, two sensors were mounted further aft to help identify when the craft is airborne. The sensors were mounted midway between the transverse frames (longitudinal position) and away from the spray rails to avoid separated flow (transverse position). Care has also been taken to ensure that the sensors' diaphragm is mounted flush with the hull bottom surface. Pressure sensor model 113B28 from PCB Piezoelectronics, Inc. was chosen for its size, high sensitivity, fast response and ruggedness. It has a measurement range of 344.7 kPa, resonant frequency ≥500 kHz and a diaphragm diameter of 5.5 mm. The sensors were calibrated by the manufacturer and the specified sensitivity for each sensor (≈14.5 mV/kPa) was used.

Local panel responses were measured using a matrix of linear strain gauges (Vishay C2A-06-125LW-350, Gauge Length 3.18 mm, Resistance 350 Ω) positioned as shown in Figure 2. The gauges were mounted at the centre of the panels i.e., the hull plating area between two consecutive longitudinal stiffeners and transverse frames, and aligned parallel to the transverse frames. In the case where pressure sensors are installed at the centre of the panel, the strain gauges were offset in the longitudinal direction by 50 mm. The underlying surface has been carefully prepared before installing the gauges following the tape-assisted method. Global hull deflections were measured using linear position sensors (Variohm VLP200, Stroke Length 200 mm) in the cabin and cockpit. The sensors were mounted on a telescopic rod to increase the distance between the measuring ends and the rod ends, marked with a cross in Figure 2, were bolted to the transverse frames.

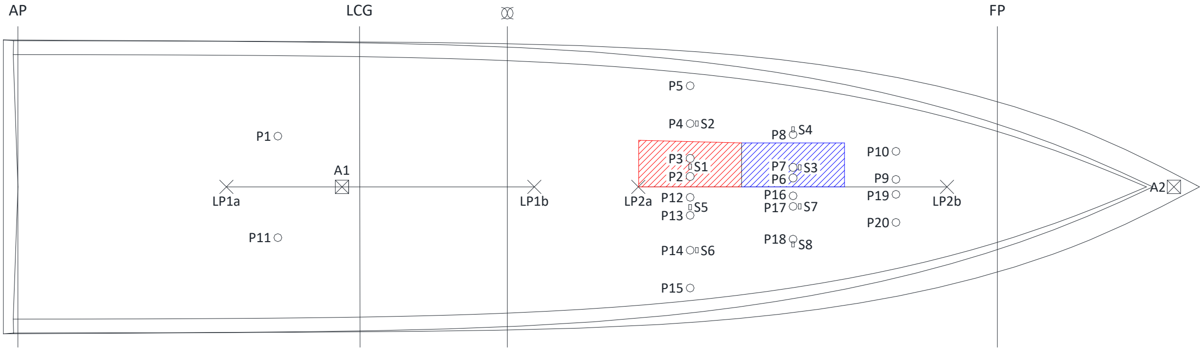

Figure 2 - Layout of the instrumentation: pressure sensors (P1 - P20), strain gauges (S1 - S8), accelerometers (A1 and A2) and linear position sensors (LP1 and LP2). The shaded areas represent the extents of panels A (red) and B (blue).

Table 2 – Longitudinal (measured from transom parallel to keel) and transverse (measured from keel parallel to hull bottom) positions of pressure sensors and strain gauges and deadrise angles of the instrumented transverse sections.

Section	Deadrise angle (°)	Sensor(s)	Longitudinal position (mm)	Transverse position (mm)
1	22	P1 (P11)	1945	410
2	28.5	P2 – P5 (P12 – P15)	5030	90, 240, 530 & 860
		S1 (S5)	5030	170
		S2 (S6)	5080	530
3	32	P6 – P8 (P16 – P18)	5800	80, 170 & 450
		S3 (S7)	5850	170
		S4 (S8)	5800	495
4	38	P9 & P10 (P19 & P20)	6570	70 & 320

The data was logged with a National Instruments (NI) data acquisition system and stored on a 32 GB Industrial grade SD card. The NI system consists of a cDAQ-9135 Controller with integrated 1.33 GHz dual-core Intel Atom processor, five NI 9234 Integrated Electronic Piezoelectric (IEPE) modules with built-in anti-aliasing filters for the pressure measurements, an NI 9236 Strain Gauge module with built-in quarter bridge completion circuits for 350 Ω strain gauges, and an NI 9205 Analog Voltage Input module to read the output voltage from the accelerometers and linear position sensors. The GPS data was logged into the controller via the serial port. The data logger and sensors were powered using two 14VDC rechargeable batteries and a voltage regulator was used to provide a stable reference voltage for accelerometers and linear position sensors. The data logger, voltage regulator and batteries were held in a waterproof and impact resistant case inside the cabin strapped to the underlying hull structure.

2.3. Wave trials

The trials were performed in the Solent, UK, near the Hayling Island Wave Buoy between July and November 2015. The wave buoy (Datawell Directional WaveRider Mk III) is operated by the Channel Coast Observatory and records several wave parameters of interest such as height, period and direction. The data is freely available to the public on the Channel Coast Observatory website (www.channelcoast.org). Three trials were performed in different sea conditions with significant wave heights ranging between 0.29 m and 0.64 m and zero crossing periods between 2.6 s and 3.8 s. In each trial the boat was operated at the highest possible safe speed for the sea state conditions based on the experienced judgement of the coxswain. The boat speeds tested range between 25 knots in the rough conditions ($H_s = 0.64\ m$) and 45 knots in moderate conditions ($H_s = 0.33m$). Multiple runs were performed in each trial. Most of the runs were done in head seas however some runs in following, beam, and quartering seas were also performed. The heading was visually estimated by the coxswain. The total number of test runs is 24 and in each run the boat was driven at constant speed and heading for at least five minutes. The sampling rate was 5.12 kHz in the first trial and 10.24 kHz in the other two, except for the GPS, which was sampled at 1Hz in all the trials. To limit the size of the data files, the data logger was set to start writing in a new file every 5 minutes.

In this paper four head sea runs covering a good range of sea and operational conditions are considered to illustrate the data processing and analysis procedures. The duration of each run is 5 minutes. The details of the runs are given in Table 3 where the mean speed values over the five minute period (± the standard deviation), significant H_s and maximum H_{max} wave heights and zero crossing periods T_z are shown. The speed coefficient C_V ranges between 2.7 and 5.2 which indicates that in all runs the boat was planing (Savitsky & Brown (1976). The present analysis will mainly focus on the acceleration, pressure and local strain data. Unfortunately, the voltage module did not work in run 3 and therefore acceleration data is not available.

Table 3 – Head sea runs studied in the present work.

Run	Date	Speed, knots	H_s, m	H_{max}, m	T_z, s
1	09/07/15	40 ± 0.3	0.29	0.43	3.1
2		45 ± 0.5	0.33	0.49	2.7
3	05/08/15	35 ± 0.6	0.39	0.43	2.9
4	20/11/15	26 ± 1.9	0.6	0.99	3.4

3. Data processing

Post-processing of the experimental data is performed using the commercial software DIAdem from National Instruments. DIAdem offers several built-in functions for signal processing and also allows the user to write code using the built-in Visual Basic script host (National Instruments 2017). The following post-processing was carried out:

1. The data files that make up a single test run are merged together and the GPS data is used to identify a five-minute segment where the speed and heading are more or less constant.
2. The voltage signals (acceleration and position) were set to have a zero offset of approximately 2.5 V. This is removed by subtracting the mean of the signal from the signal using the Offset Correction function available in DIAdem. The signals are then converted from voltage to acceleration and displacement respectively using the manufacturer-specified sensitivity of the sensors and low-pass filtered as discussed in 3.1.
3. The baseline drift in the strain signals is removed using the algorithm described in 3.2.
4. The pressure and strain peaks are identified using the algorithm described in 3.3.
5. Histograms of the pressure and strain peaks and other quantities of interest such as the average of the largest 1/3rd and 1/10th peaks are calculated.
6. Analytical distributions are fitted to the samples of pressure and strain peak values and extreme values are estimated.

3.1. Low pass filtering

Figure 3 shows a short segment of typical unfiltered vertical bow acceleration response recorded in run 2 where five separate wave impact events can be observed. The impacts are characterised by a rapid increase in acceleration followed by high frequency and large amplitude oscillations. The oscillations damp out prior to the next impact, which means that each impact can be considered independent of the others and analysed separately (Riley et al. (2014), Savitsky (2016)).

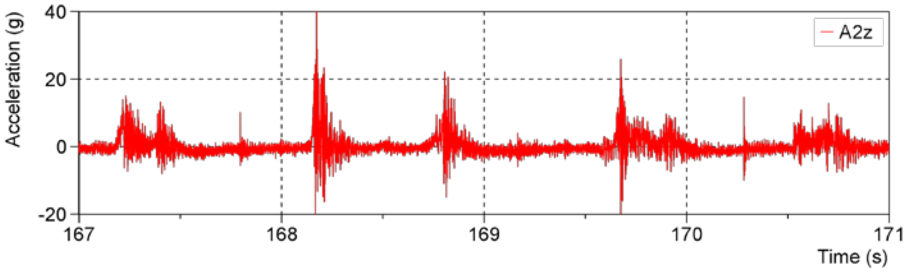

Figure 3 - Characteristic unfiltered vertical acceleration response measured at the bow, run 2.

The Fourier spectrum of the unfiltered vertical bow acceleration signal recorded in run 2 is presented in Figure 4. The spectrum shows a large peak near 1 Hz which represents the rigid-body interaction with waves and several lower amplitude peaks across a range of frequencies from roughly 50 Hz to 500 Hz that are most likely due to structural vibrations caused by wave impacts and engine noise (Riley et al. 2014). The high-frequency vibration content can be removed by low pass filtering the raw signal. Figure 5 compares the raw signal with low-pass filtered signals at different cut-off frequencies for the impact event at time ≈168 s. A 10th-order Butterworth filter is used. The results show that with decreasing the cut-off frequency more high frequency vibration content is removed and the magnitude of peak acceleration decreases. The 10 Hz cut-off frequency recommended by Riley et al. (2014) is too low and does not capture the sharp acceleration rise accurately. The 30Hz low-pass filter is found to effectively remove the high frequency content without significantly affecting the rigid body response and is chosen in the present work. Similar observations were made for the cockpit acceleration signal and other runs.

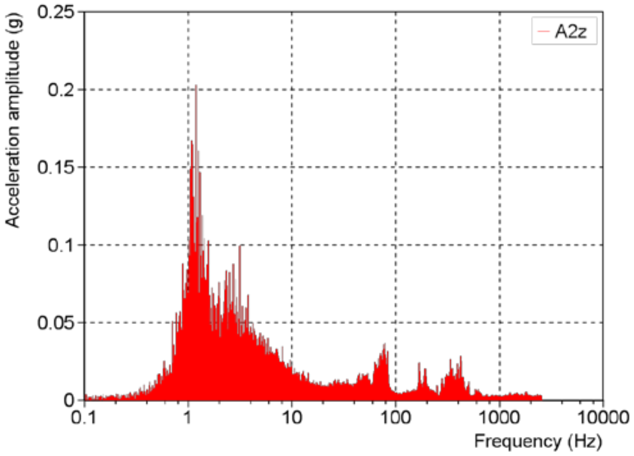

Figure 4 - Fourier spectrum of the raw bow vertical acceleration signal, run 2.

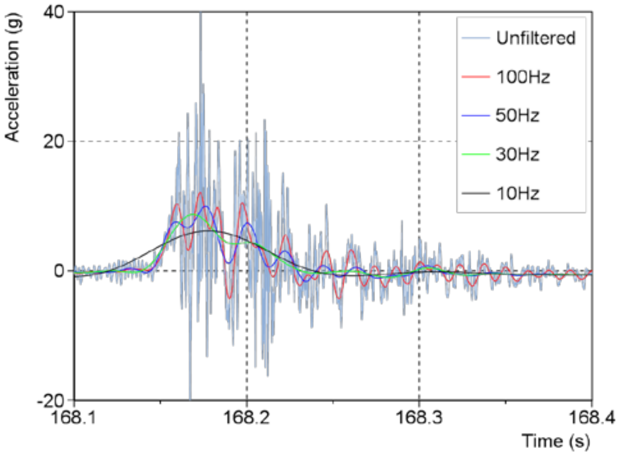

Figure 5 - Effect of cut-off frequency on the acceleration data.

3.2. Baseline correction

The strain signals contain undesirable baseline drift that is removed by subtracting a baseline estimate from the signal as follows.

1. Low pass filter the raw signal at 50 Hz with a 10th-order Butterworth filter to remove high frequency noise.
2. Differentiate the filtered signal to accentuate the high rates of change associated with impacts and attenuate the intervals in between.
3. Search for the 'flat' intervals between impacts in the signal derivative – the intervals in which the values of the signal derivative are in a specified window – and remove intervals of short duration which generally result from inflection points or local maxima/ minima in the strain signals. For each interval identified calculate the mean of the signal and the time midpoint.
4. Fit a line to the data points (calculated means and midpoints) to obtain the baseline estimate and subtract it from the raw strain signal.

Figure 6 shows an example of application of this algorithm to signal S1. The cut-off frequency used to filter the strain signals is higher than that chosen for the acceleration signals mainly because the strain rise times are typically shorter than the acceleration rise times and, hence, higher frequency is required to accurately capture the strain rise, which is important here.

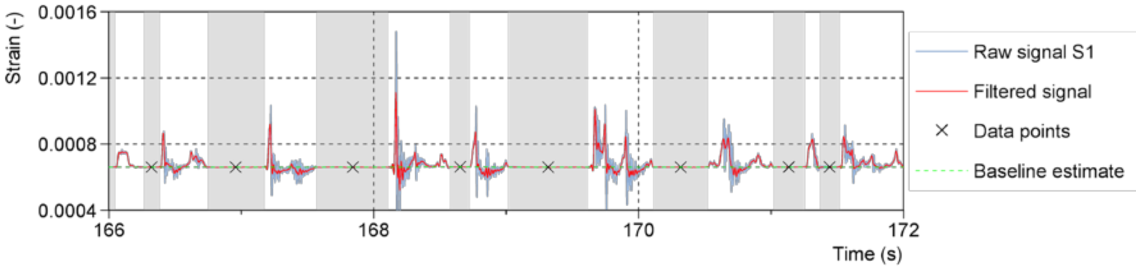

Figure 6 - Baseline correction algorithm applied to signal S1, run 2.

3.3. Peak identification

The peaks in the pressure and strain signals are identified by first identifying the impact events in the signals and then searching for the peak within each event. The characteristics of the signals, in particular the rapid increase in pressure and strain associated with water impact, are used to identify the impact events. With this approach identified impact events can also be extracted from the signal for comparisons with for instance, numerical predictions or drop test measurements. The algorithm for identifying the peaks in the pressure and strain signals is as follows.

1. Low pass filter the signal with a 10th-order Butterworth filter and 100 Hz cut-off frequency to remove the high frequency noise. This step is only applied to the strain signals; the pressure signals contain less noise, particularly between impacts.
2. Differentiate the signal to accentuate the high rates of change associated with impacts and attenuate the intervals in between (see Figure 7a).
3. Search for the 'flat' intervals between impacts in the signal derivative and remove intervals of short duration (peaks/ valleys; pressure signals: duration ≤ 10 ms; strain signals: duration ≤ 5ms) which generally result from inflection points or local maxima/ minima in the noisy signals. The search results are stored as a binary signal (shaded areas in Figure 7a).
4. Invert the binary signal to obtain the impact events.
5. Remove gaps between impact events and impact events of short duration from the search results,
    a. Remove gaps of duration ≤ 100 ms (see Figure 7c).
    b. Calculate the duration of each impact with a maximum value greater than the root mean square (RMS) of the signal and the mean duration.
    c. Filter out short impact areas. In the case of the pressure signals, remove impacts of duration ≤ 50 ms from signals with mean duration ≥ 100 ms (see Figure 7d). In the case of the strain signals remove impacts of duration ≤ 120 ms if the mean duration > 200 ms and ≤ 60 ms otherwise.
6. Search for the maximum in each area, i.e. here referred to as the peak, and output the magnitude and time. It should be noted that the maximum peak is not necessarily the first one. The circles in Figure 7d represent the identified peaks.
7. Sort the peaks in ascending order and remove peaks of magnitude less than the signal RMS.

The threshold values were selected from testing the algorithm on the four data sets and were found to accurately identify the impact events and peaks which would have been identified manually. Figure 7 shows an example of application of the peak identification algorithm to signal P2 from run 2.

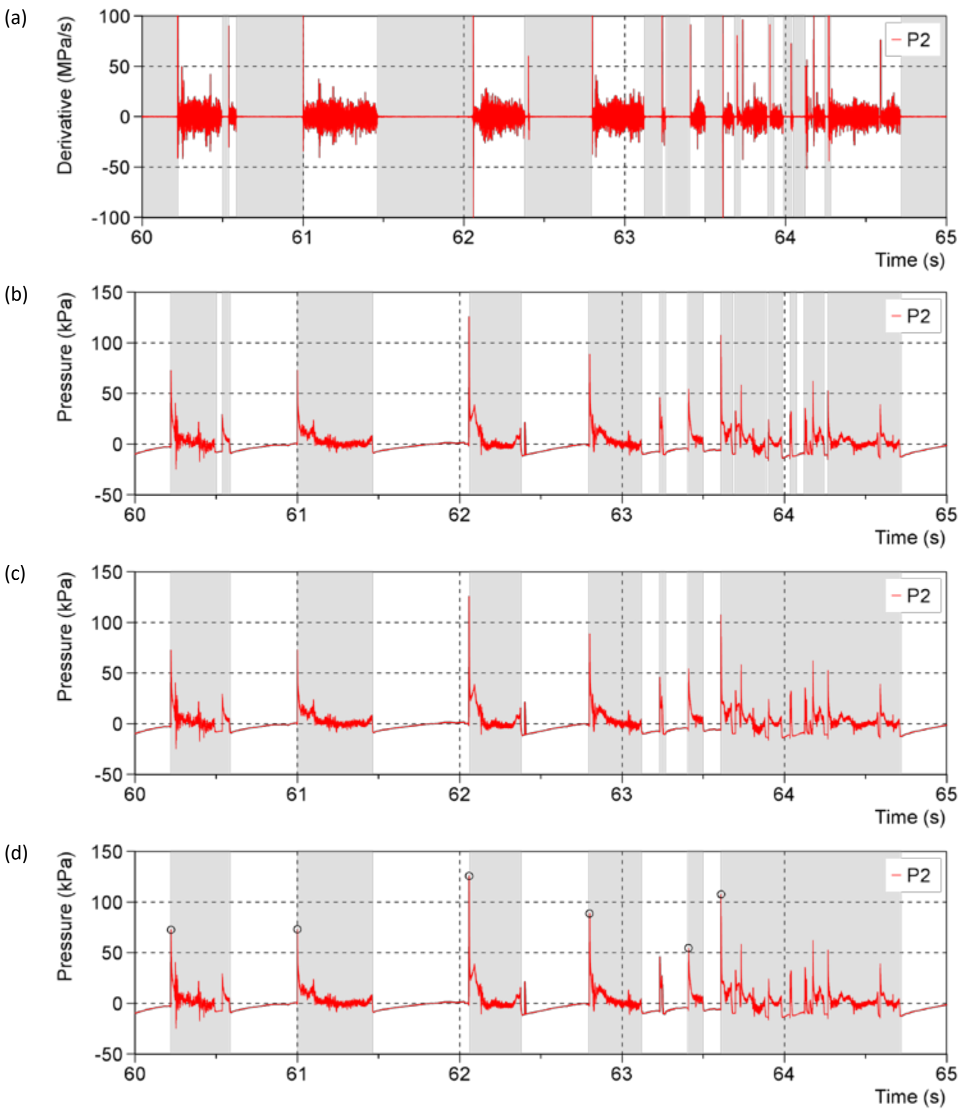

Figure 7 - Peak identification algorithm applied to signal P2, run 2: (a) signal derivative and 'flat' intervals identified, (b) pressure signal and impact areas identified, (c) impact areas with short gaps filtered out, and (d) impact areas with short peaks filtered out and identified peaks.

4. Statistical methods and distributions

Let $x_{(1)}, x_{(2)} \dots, x_{(n)}$ be an ordered sample of independent and identically distributed data of size n with cumulative distribution function $F(x)$. From order statistics, the cumulative distribution function $F_e(x)$ of the extreme value $x_{(n)} = \max\{x_{(1)}, x_{(2)}, \dots, x_{(n)}\}$ is related to $F(x)$ by (Ochi 1981),

$$F_e(x) = F^n(x) \tag{1}$$

and the probability α of exceeding a characteristic extreme value x_α is (Ochi 1981),

$$P[response > x_\alpha] = \alpha = 1 - F^n(x_\alpha). \tag{2}$$

Considering that α is small and n is large,

$$F(x_e) = (1-\alpha)^{\frac{1}{n}} \approx 1 - \frac{\alpha}{n}. \tag{3}$$

Characteristic extreme values with low probability of exceedance can therefore be estimated if the cumulative distribution function of the sample $F(x)$ is known. In the present work, two analytical models are fitted to the sample of peak values to approximate $F(x)$, namely the two-parameter Weibull and the Generalized Pareto distributions. The goodness of fit of Weibull and Generalized Pareto models to the peak value distributions is examined using Quantile-Quantile plots and the root mean square error (RMSE) statistic written as,

$$RMSE = \sqrt{\frac{1}{n}\sum_{i=1}^{n}(x_i - \hat{x}_i)^2} \tag{4}$$

where x_i and $\hat{x}_i$ are the measured and estimated peaks at the same quantile level, respectively. The RMSE is normalized using the mean of the measured data to enable comparisons between data sets with different scales.

4.1. Weibull distribution

The cumulative distribution function of the two-parameter Weibull distribution is given by,

$$F(x;a,b) = 1 - e^{-\left(\frac{x}{a}\right)^{b}} \tag{5}$$

where a and b are the scale and shape parameters respectively. The Rayleigh and Exponential distributions are both special cases of Weibull distribution corresponding to $b = 2$ and $b = 1$ respectively.

4.1.1. Weibull parameters estimation and threshold selection

The parameters of the Weibull distribution are estimated using the least squares method. Taking the natural logarithm of equation (5) twice,

$$\ln\left[-\ln\left(1 - F(x)\right)\right] = bln(x) - bln(a) \tag{6}$$

Is obtained which represents a linear relationship between $\ln\left[-\ln\left(1 - F(x)\right)\right]$ and $\ln(x)$ with slope b and y-intercept $-\,b\ln(a)$. Thus, the shape and scale parameters can be estimated by least-square fitting equation (6) to the data where the cumulative probability associated with each observation is $F(x) = i/(n+1)$ for $x_{(i)} \leq x < x_{(i+1)}$ (Coles 2001).

To better capture the tail of the distribution a threshold value is introduced and the Weibull distribution is only fitted to the peak values above the threshold. The procedure for choosing the optimal threshold value and estimating the Weibull parameters is similar to that presented in Razola et al. (2016) and is as follows,

1. Sort the sample of peak values in increasing order and for each peak value calculate the cumulative probability, $\ln\left[-\ln\left(1 - F(x)\right)\right]$ and $\ln(x)$.
2. Let $u_1 < u_2 < \cdots < u_m$ be a range of suitable threshold values.
    a. For each threshold value, use the least squares method to fit a straight line on the transformed axes to the peaks above the threshold and calculate the coefficient of determination (R^2 statistic).
    b. Choose the threshold value that yields the maximum R^2 value.
3. Calculate the shape and scale parameters from the slope and intercept of the fitted line.

4.1.2. Extreme value

The extreme value with probability of exceedance α is obtained by substituting equation (5) into (3) resulting in,

$$x_e = a\left[\ln\left(\frac{n}{\alpha}\right)\right]^{\frac{1}{b}}. \tag{7}$$

The most probable extreme value, defined as the extreme value most likely to occur in n observations, is obtained by setting $\alpha = 1$.

4.2. Peak-Over-Threshold method

The cumulative distribution function of the peaks over a high threshold u is,

$$F_u(x) = P(X \le x | X > u) = \frac{F(x) - F(u)}{1 - F(u)} \tag{8}$$

and is related to the distribution function of the excesses, $F_{x-u}(x-u)$, by,

$$F_{x-u}(x-u) = F_u(x). \tag{9}$$

Pickands (1975) showed that for large enough threshold the distribution of excesses is well approximated by the Generalized Pareto distribution. The cumulative distribution function of the Generalized Pareto distribution (GPD) is given by,

$$G(x; c, \lambda) = \begin{cases} 1 - \left(1 + \frac{cx}{\lambda}\right)^{-\frac{1}{c}} & c \neq 0 \\ 1 - e^{-\frac{x}{\lambda}} & c = 0 \end{cases}. \tag{10}$$

The parameters c and λ are the shape and scale parameters, respectively, and the support is $0 \le x < \infty$ for $c \ge 0$ while for $c < 0$ the support is $0 \le x \le -\lambda/c$. The case $c = 0$ represents the exponential distribution with mean λ, $c > 0$ indicates a heavier tail than the exponential one (sub exponential), while $c < 0$ implies a lighter tail (super exponential).

4.2.1. Threshold selection and GPD parameters estimation

The choice of the threshold requires balancing bias and variance – the threshold needs to be sufficiently high for the asymptotic approximation to be valid, thus reducing the bias; however a high threshold implies smaller samples of excesses, which increases the variance in the parameter estimates. The GPD satisfies a threshold stability property: if for a particular threshold u_o the excesses follow a GPD then, for higher thresholds ($u > u_o$) the shape and normalised scale ($\lambda^* = \lambda - cu$) parameter estimates should tend to constant values (Coles 2001). These properties are used to choose the threshold value. The approach is to estimate the shape and scale parameters for a range of thresholds and examine their variation with threshold.

The GPD parameters are estimated using the Method of Moments (MOM), that is, the sample mean and variance are equated to the analytical moments of the GPD resulting in,

$$c = \frac{1}{2}\left(1 - \frac{\bar{x}^2}{s^2}\right) \tag{11}$$

$$\lambda = \frac{1}{2}\bar{x}\left(\frac{\bar{x}^2}{s^2} + 1\right) \tag{12}$$

where $\bar{x}$ and s^2 are the sample mean and variance, respectively. The MOM may produce non-feasible estimates, in the sense that there are samples for which c is negative and the peak magnitudes are larger than the upper limit for the GPD, i.e., $x > -\lambda/c$. The hybrid-MOM of Dupuis & Tsao (1998) is always feasible and is used in the present study. This hybrid estimator takes the values of the MOM estimator if the results are feasible and sets $c = -\lambda/x_{(n)}$ otherwise.

The automated procedure developed for choosing the threshold is as follows,

1. Let $u_1 < u_2 < \cdots < u_m$ be a range of suitable threshold values. For each threshold u calculate the shape and scale parameters using the Hybrid-MOM.
2. Fit a non-parametrical approximating spline to the shape parameter curve. The x-range (threshold range) is divided into twenty equidistant sections and in each section a straight line is fitted to the data using the least square error method.
3. Calculate the forward difference derivative of the spline curve and normalize the derivative signal using the range of the threshold values.
4. Search the sections in which the derivative is within specified low limits and filter out areas (clusters of adjacent sections) with two sections or less.
    a. If the search returns zero areas select the 0.8-quantile as the threshold.
    b. If several areas are identified (the shape parameter plot reaches multiple plateaus) select the area with the largest number of sections. If two areas have equal number of sections, select the area that corresponds to the larger threshold.
    c. The threshold is the minimum value of the chosen area.

4.2.2. Extreme value

From equations (3) and (10) the extreme value x_e with a probability of exceedance α is,

$$x_e = \begin{cases} u + \dfrac{\lambda}{c}\left[\left(\dfrac{k}{\alpha}\right)^c - 1\right], & c \neq 0 \\ u + \lambda \ln\left(\dfrac{k}{\alpha}\right), & c = 0 \end{cases} \tag{13}$$

where k is the number of peaks above the threshold u and $F(u) = (n-k)/n$.

5. Results and discussion

5.1. Characteristic results

In Figures 8 - 10 segments of typical acceleration, pressure and strain time series are presented. The craft was travelling into head seas at 45 knots with significant wave height $H_s = 0.33\ m$ and zero crossing period $T_z = 2.7\ s$ – run 2. The acceleration signals are low pass filtered with a 10th-order Butterworth filter and a cut-off frequency of 30 Hz as discussed in section 3.1. The pressure and strain peaks identified using the algorithm described in section 3.3 are also included. The signals consist of repeated hull-water impacts with each impact having different characteristics, such as, shape of the signal, peak magnitude, rise and decay time and impact duration. For a high-speed planing craft travelling in waves the trim angle, vertical velocity, deadrise angle and wave geometry are different for each individual hull-water impact and as a result each event is unique (Allen & Jones (1978), Savitsky (2016)). The rise and decay times are typically of the order of a few milliseconds and duration of impact events is generally less than 0.5 seconds. Example histograms of the pressure and strain peaks are presented in Figure 11. The distributions are generally skewed to the right with low magnitude peaks occurring frequently and few large magnitude peaks, some of which differ greatly from the other observations – see for instance the distribution for S2 in Figure 11. The largest pressure peak was measured at P6 during run

2 and has a magnitude of 342 kPa and the largest strain peak is 1182 μs measured at S3 during run 4. In comparison, the largest pressure peak measured by Garme & Rosén (2003) was 370 kPa at maximum speed of 35 knots and significant wave height greater than 1m, whilst Mørch & Hermundstad (2005) measured average pressures of about 140 kPa and strains of about 4000 μs at a speed of around 30 knots and significant wave height of 0.55 m.

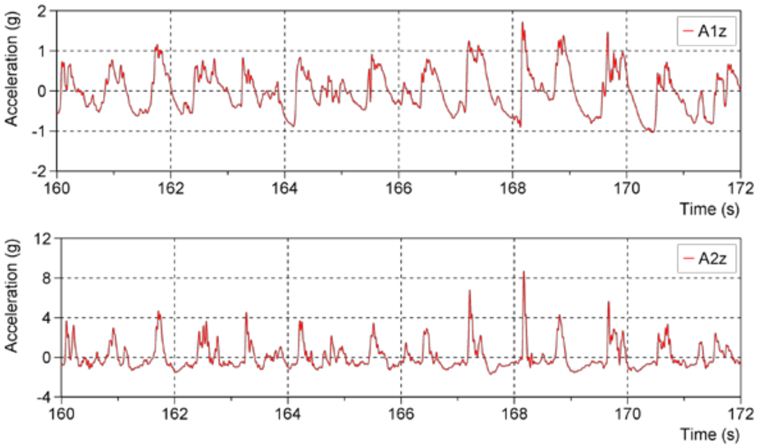

Figure 8 - Characteristic time series of cockpit (A1z) and bow (A2z) acceleration, run 2.

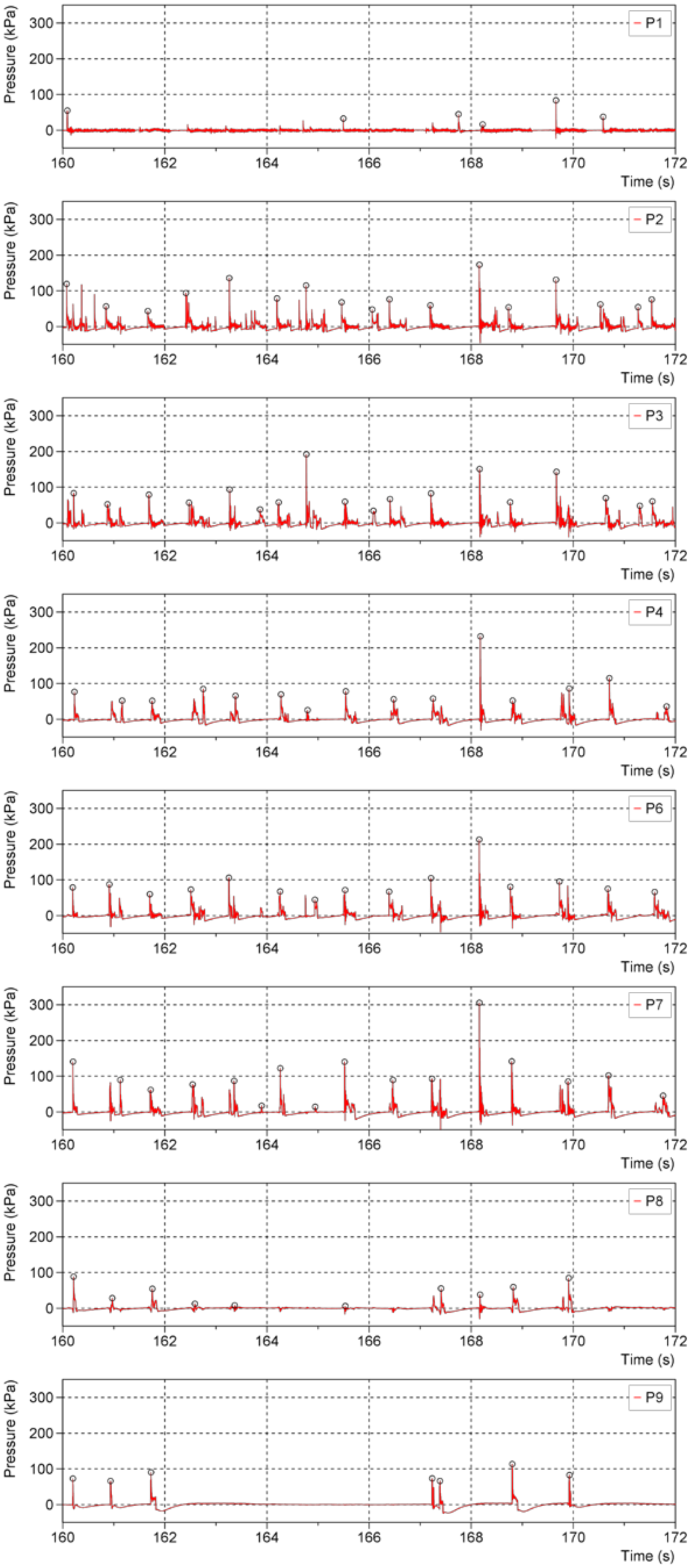

Figure 9 - Characteristic time series of pressure and identified peaks, run 2.

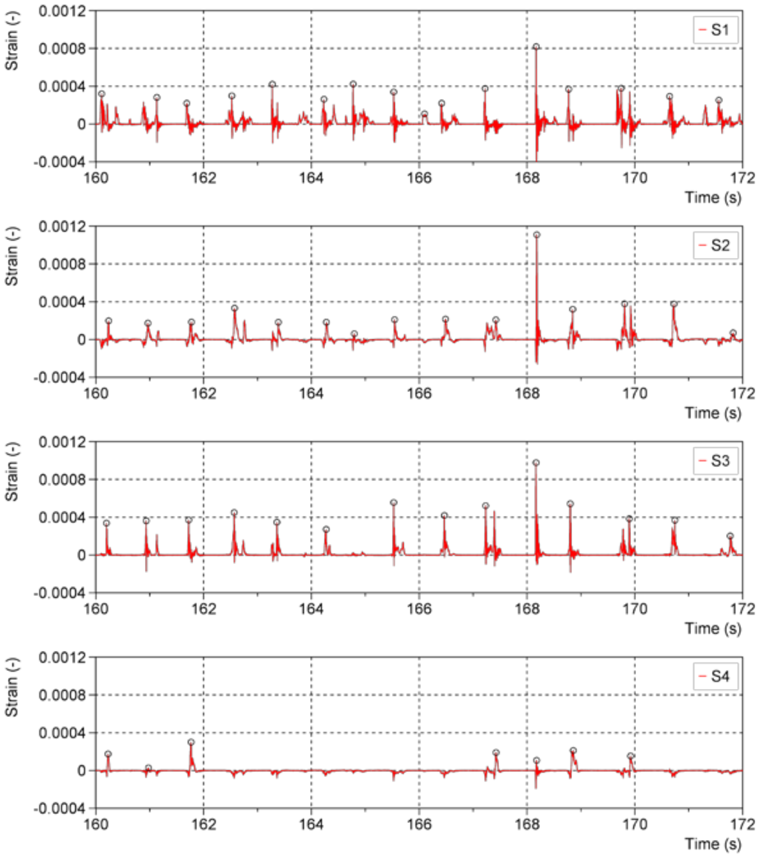

Figure 10 - Characteristic time series of strain and identified peaks, run 2.

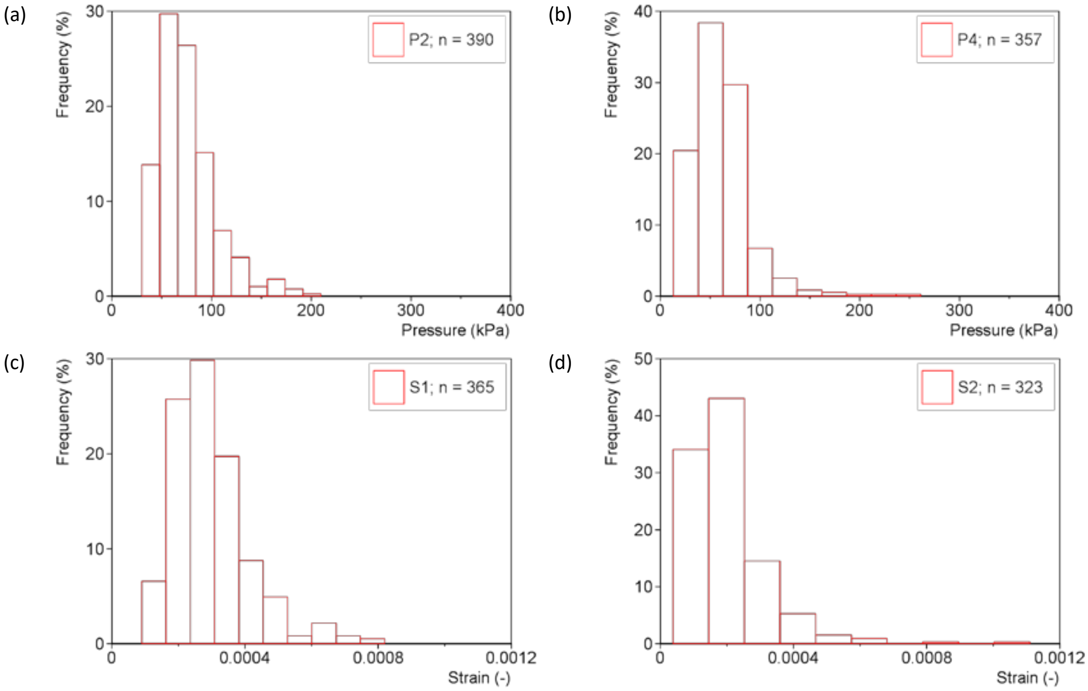

Figure 11 – Characteristic histograms of pressure (a, b) and strain (c, d) peaks, run 2.

The number of peaks identified in each pressure and strain signal for all runs are reported in Tables 5 and 6. The impacts are fairly symmetric in terms of the number of peaks recorded on port and starboard sides, particularly for the sensors located near the keel. Furthermore, the number of impacts recorded by the sensors located near the chine and most forward, i.e., sensors P5, P8, P9, P10 and S4 and corresponding sensors on the starboard side, is significantly lower. As can be seen, the peak identification algorithm developed in the present work accurately identifies the peaks in all pressure and strain signals considering that the duration of the interval between impacts and the duration of impacts varies within each signal and also between signals. By accurately we mean that the algorithm identifies the peaks that would have been chosen manually. This is because our algorithm uses the characteristics of the actual signal to define the search area (impact events), i.e., the rapid changes in pressure and strain associated with impact and the intervals of nearly zero pressure/ strain in between events. The peak is then taken as the maximum pressure or strain during that time interval. There are, however, impact events that are characterised by multiple peaks (the time duration between these peaks is very short otherwise the algorithm would assume two events) and the algorithm only considers the maximum value as the peak. The physical mechanism behind these multiple peaks is difficult to explain without knowing the relative velocity of the craft, free surface profile and so on. It is also noted that the horizontal threshold method commonly used to identify the acceleration peaks (see e.g. McCue (2012), Riley et al. (2013) and Razola et al. (2016)), which uses a constant sliding time window calculated from the wave encounter frequency to search for the peak, would identify false peaks in this case.

The averages of the largest 1/3rd and 1/10th pressure and strain peaks are presented in Figure 12 and Tables 7 – 10. The ratio of the average of the largest 1/3rd pressure and strain peaks to the average of the largest 1/10th is typically between 0.6 and 0.8 for all samples and runs. While the number of impacts recorded on port and starboard sides agree relatively well, the peak magnitudes show some differences. In particular, the pressure and strain peaks recorded on the port side, i.e. sensors P1-P10 and S1-S4, are larger than the starboard side peaks except for run 3 where no clear trends are observed. This is most likely due to wave energy spreading, making it difficult for the coxswain to judge if it was truly head sea. The averages of the largest 1/3rd and 1/10th also provide insight into how the magnitude of the loads and responses varies across the hull bottom surface. As can be seen, the largest peaks are recorded by the sensors located near the keel i.e. sensors P2, P3, P6, P7, P9 and the corresponding starboard side sensors, and the magnitude of pressure generally decreases with increasing distance from the keel towards the chines. The pressures measured by the second row of sensors, i.e. sensors P6 – P8 and P16 – P18, however, don’t follow this trend. In particular the pressure peaks measured at P17 are for all runs greater than the P16 peaks while the P7 peaks are greater than the P6 peaks for runs 1 and 2. Furthermore, the strains measured on the panels next to the keel, i.e., S1, S3, S5 and S7, are larger than strains measured on the adjacent panels for all runs. It is noted that the design rules assume the pressure to be uniformly distributed across the hull bottom; however, in reality the magnitude of pressure decreases from keel to chine. Comparing the averages of the largest 1/3rd and 1/10th for runs 1 and 2 (high forward speed and moderate seas) with those for run 4 (moderate speed and rough seas) it can be observed that larger pressures and strains were measured when the boat was travelling at high speed.

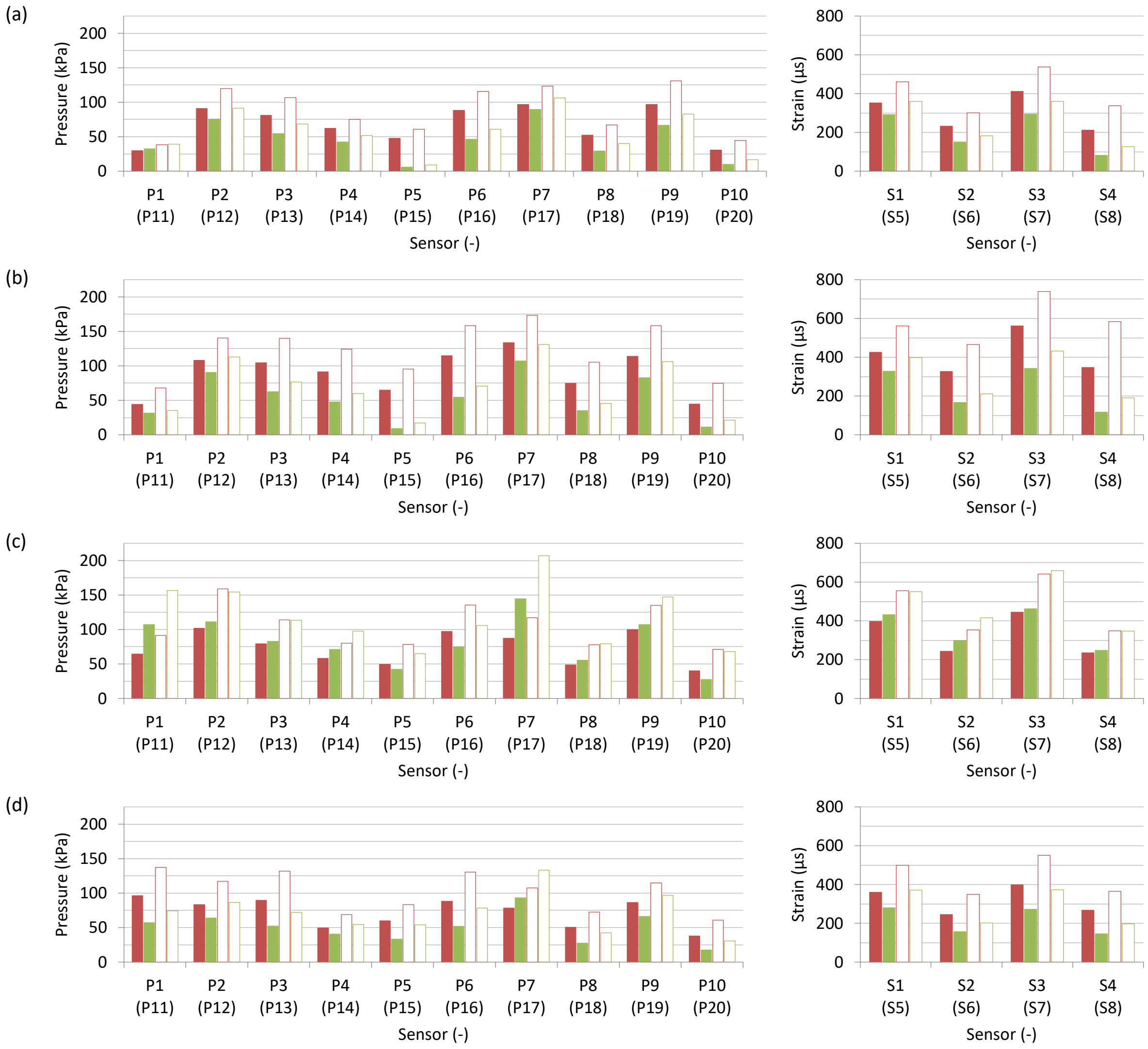

Figure 12 - Average of largest 1/3rd (filled bars) and 1/10th (empty bars) pressure and strain peaks for P1–P10 and S1–S4 (red) and P11-P20 and S5-S8 (green), runs 1-4 (a – d).

Figure 13 shows the cockpit and bow vertical accelerations responses recorded during the impact event at time ≈ 168s, which is the most severe impact recorded in run 2. Prior to impact (t = 168.135s - marked with a red vertical line in Figure 13) the cockpit accelerometer records a fairly constant acceleration of about - 0.7g, which suggests that the craft is moving downwards but is not in free-fall condition – it is most likely that the craft is pitching downwards with the stern in the water. Riley et al. (2014) categorise such event as 'Type Charlie Slam' where the energy of impact is mainly due to the relative forward velocity between the craft and incident wave, and has little to do with significant vertical drop at the LCG. This is further supported by the fairly low pressure measured at P1 - see Figure 9 – which suggests that the stern was in the water. At time = 168.135s the craft impacts the incident wave and the acceleration in the cockpit and at the bow rises sharply and reaches a maximum of 1.7 g and 8.7 g, respectively. The cockpit and bow acceleration rise times are 38 ms and 34 ms, respectively.

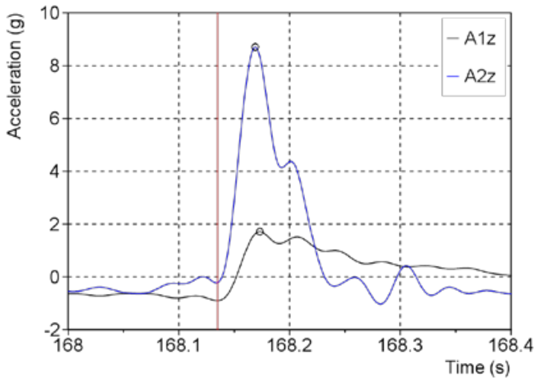

Figure 13 - Cockpit (A1z) and bow (A2z) acceleration responses recorded during the impact event at t ≈ 168s, run 2. The time of impact and maximum cockpit and bow accelerations are marked by the vertical red line and markers, respectively.

The pressures and strains recorded by sensors P2 – P4, P6 – P8 and S1 – S4 during this particular impact event are presented in Figure 14. The signals are plotted based on the longitudinal and transverse (relative to the longitudinal stringers) location of the sensors - see Figure 15. As the boat enters the water a high pressure pulse located at the intersection between the hull bottom and water surface, also known as the spray root, rapidly propagates across the hull bottom surface from the keel towards the chine over the instrumented area – see Figure 14 where the first peak is recorded by the sensors located next to the keel, i.e., P2 and P6 and the sensors located further out record the peak later in time.

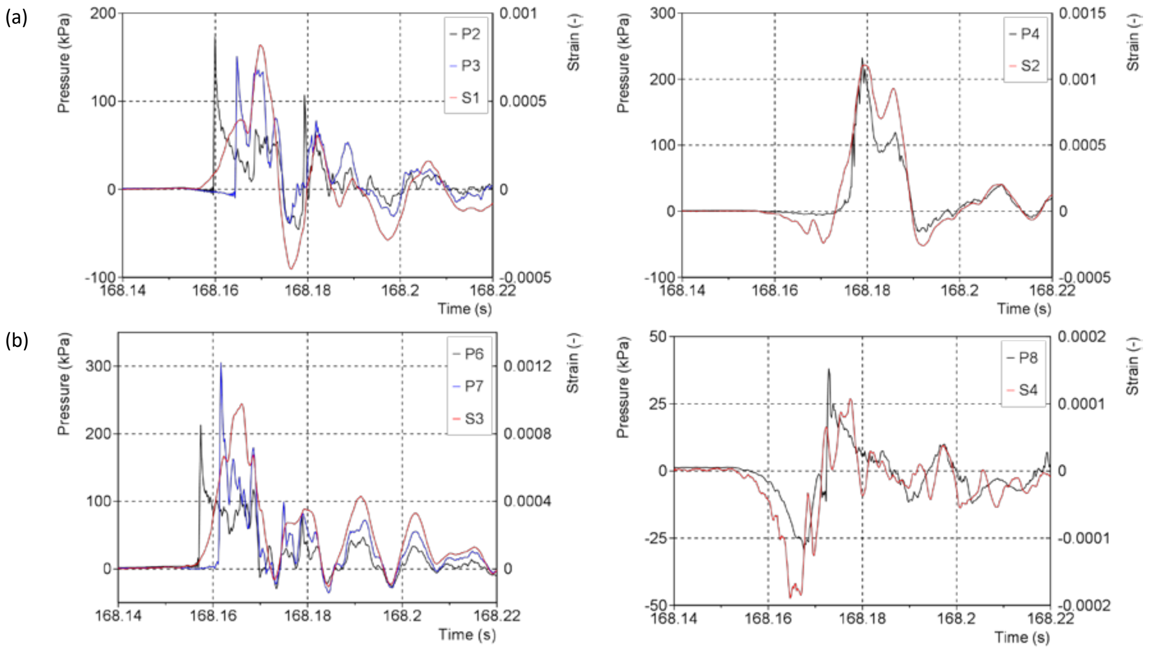

Figure 14 – Pressure and strain signals recorded by the first (a) and second (b) row of port side sensors during the impact at t ≈ 168s, run 2.

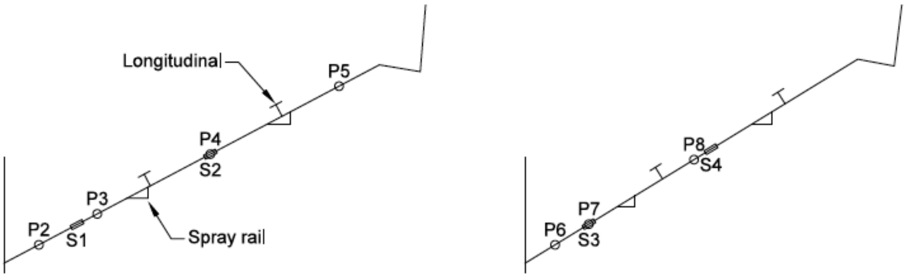

Figure 15 – Schematic illustration of the hull sections showing the relative position of the pressure sensors (P2 – P8), strain gages (S1 – S4), longitudinal stiffeners and spray rails.

The pressure signals are characterised by a sharp rise and large initial peak rapidly decaying to a lower residual pressure level. The rise time is in the order of 0.5 ms, which implies that the sampling frequency of 5.12 kHz is too low for this extreme event. The strains measured on the hull bottom area between the keel and the first longitudinal stringer i.e., S1 and S3, are characterised by a moderate rise (compared to the pressure rise time) and large initial peak followed by large amplitude oscillations about a much lower residual strain level. The panels begin to deflect inwards (positive strain) at about the same time sensors P2 and P6 record their peaks. The strains measured on the hull bottom area between the two longitudinal stringers i.e., S2 and S4, show a negative initial peak followed by a rapid increase to a positive peak. The negative peak occurs at the time of maximum S1 and S3 strain respectively which suggests that as the panel area between the keel and first longitudinal stringer is deflecting inwards, the longitudinal stringer acts as a pivot and the panel area between the two stringers deflects outwards. It can also be observed that the pressures and strains correlate quite well, particularly the shape of the signals following the peak.

5.2. Statistical results (extreme values)

In the present work the Weibull and Generalized Pareto models are only fitted to samples containing more than 200 pressure or strain peaks to limit the variance of the parameter estimates. The number of candidate thresholds in the Weibull and Generalized Pareto threshold selection algorithms is $m = 50$ and u_1 and u_m are set as the 0.4 and 0.9 quantiles of the sampled peak values, respectively. This implies that in the extreme case of the 0.9 quantile at least 20 peaks are used to estimate the model parameters.

Figure 16 shows examples of the Weibull threshold selection algorithm applied to samples of pressure and strain peaks. The first column presents the transformed sample distribution (step 1 of the procedure in 4.1.1) and the transformed Weibull model fitted to the peaks above the chosen threshold using the least squares method. The second column presents the variation of the Weibull shape parameter b and R^2 statistic with threshold value. The vertical line represents the chosen threshold value corresponding to the maximum R^2 value. As can be seen the slope of the transformed sample distributions, which corresponds to the Weibull shape parameter, changes with increasing threshold suggesting that the peaks on different levels belong to different statistical distributions. More specifically, the slope becomes less steep and the shape parameter decreases with increasing threshold suggesting that the largest peaks, which are most likely related to extreme slamming impacts, are more nonlinear. This is generally the case for both pressure and strain peak samples with very few exceptions, and justifies the use of a threshold to accurately capture the largest peaks. VanDerwerken & Judge (2017) have shown that failing to account for data truncation (step 7 in section 3.3; peaks of magnitude less than the RMS of the signal removed) can have a significant influence on the shape of the transformed sample distribution. We examined this influence of data truncation and found that for most samples this effect is small. This is mainly due to the fact that the number of peaks of magnitude less than the signal RMS is generally low (typically less than 10% of the sample size).

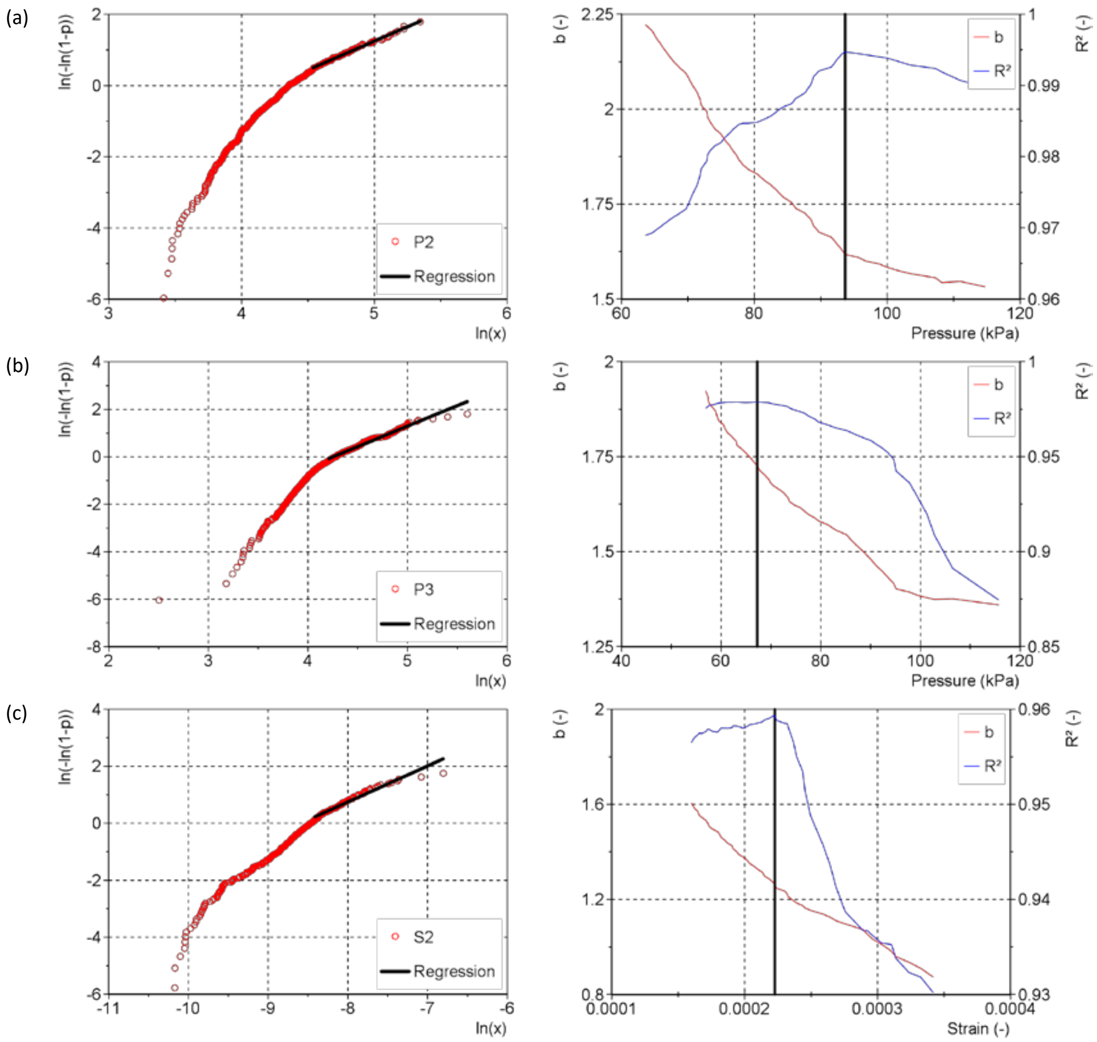

Figure 16 - Weibull threshold selection algorithm applied to peak samples P2 (a), P3 (b) and S2 (c), run 2.

Examples of application of the GPD threshold selection algorithm to pressure and strain peak samples are presented in Figure 17 where the variation of the estimated GPD shape parameter with threshold and the non-parametric approximating spline curve are shown. The vertical line represents the threshold chosen by the algorithm. The shape parameter estimates should be constant above the threshold at which the GPD model becomes valid. In practice, however, due to the relatively small sample sizes, the plots will not look constant even when the GPD model becomes valid. The GPD shape parameter estimates were found to vary quite significantly over the range of thresholds considered for many of the peak samples, particularly the strain peak samples and including peak sample P2 in Figure 17. In such event the algorithm selects the 0.8 quantile as the threshold value. The 0.8 quantile level was determined by assessment of the shape parameter stability plots for all peak samples where it was found that above this level the parameter estimates typically become highly unstable. For peak samples P3 and S2 the shape parameter appears to reach a near-constant value in the low threshold range and the algorithm selects the starting point of the identified area as threshold (step 4 of the procedure in 4.2.1).

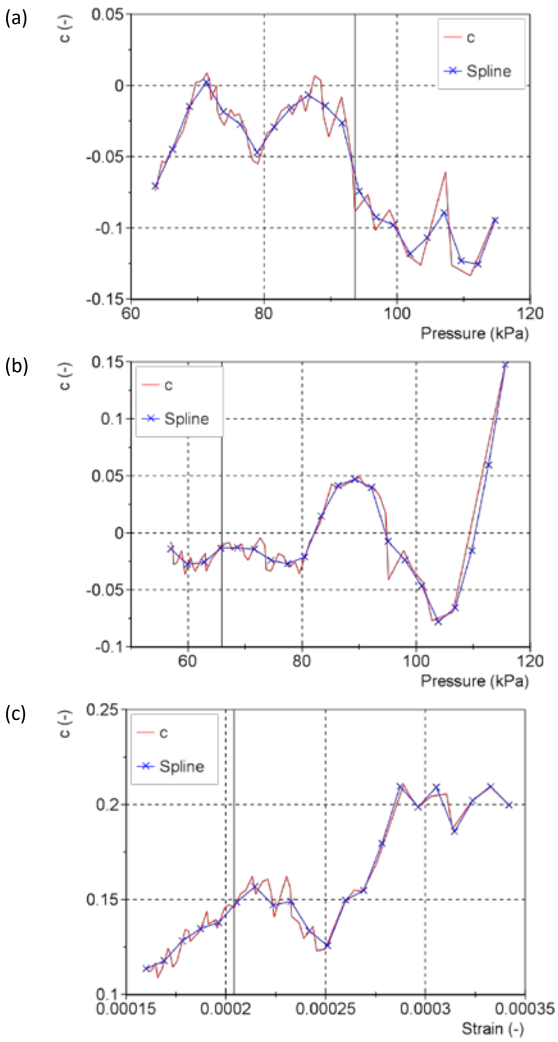

Figure 17 - GPD threshold selection algorithm applied to peak samples P2 (a), P3 (b) and S2 (c), run 2.

In Figures 18 and 19 characteristic cumulative distributions of pressure and strain peaks and fitted Weibull and Generalized Pareto models and corresponding Quantile-Quantile plots are presented. The Weibull and Generalized Pareto shape and scale parameters are presented in Figure 20 and Tables 11 - 14. The number of peaks used in the Weibull and Generalized Pareto fittings range from approximately 30 to 270. The Weibull shape parameter values range between 0.74 and 2.94 for the pressure distributions and 0.93 and 2.48 for strain distributions. However, most of the pressure and strain peak distributions fall between the exponential (b = 1) and Rayleigh (b = 2) distributions, particularly the peak samples for runs 3 and 4. Furthermore, for runs 1 and 2, the shape parameter is typically greater than two for the starboard side peak samples containing lower magnitude peaks - see Figure 12. Shape parameter value greater than 2 implies that the distribution tail is lighter than the tail of the Rayleigh distribution and indicates small nonlinearity. The GPD shape parameter values range between -0.41 and 0.25 for the pressure distributions and -0.44 and 0.16 for the strain distributions. In general, for runs 1 and 2 the GPD shape parameter is near or less than zero for both pressure and strain peaks, implying that the distributions are light-tailed, while for runs 3 and 4 the GPD shape parameter is typically positive implying that the distributions are heavy-tailed.

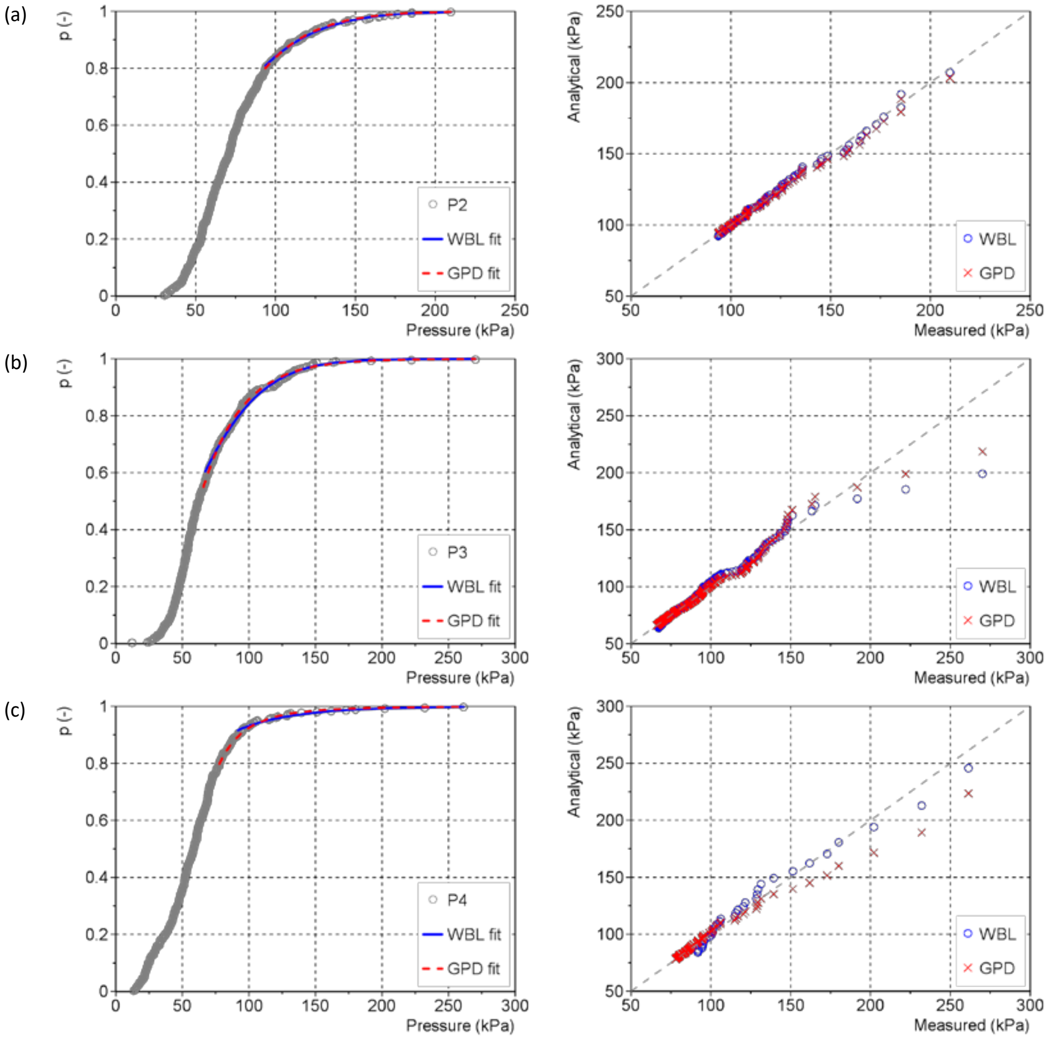

Figure 18 – Cumulative distributions of pressure peaks and fitted analytical models and corresponding Quantile-Quantile plots for peak samples P2 (a), P3 (b) and P4 (c), run 2.

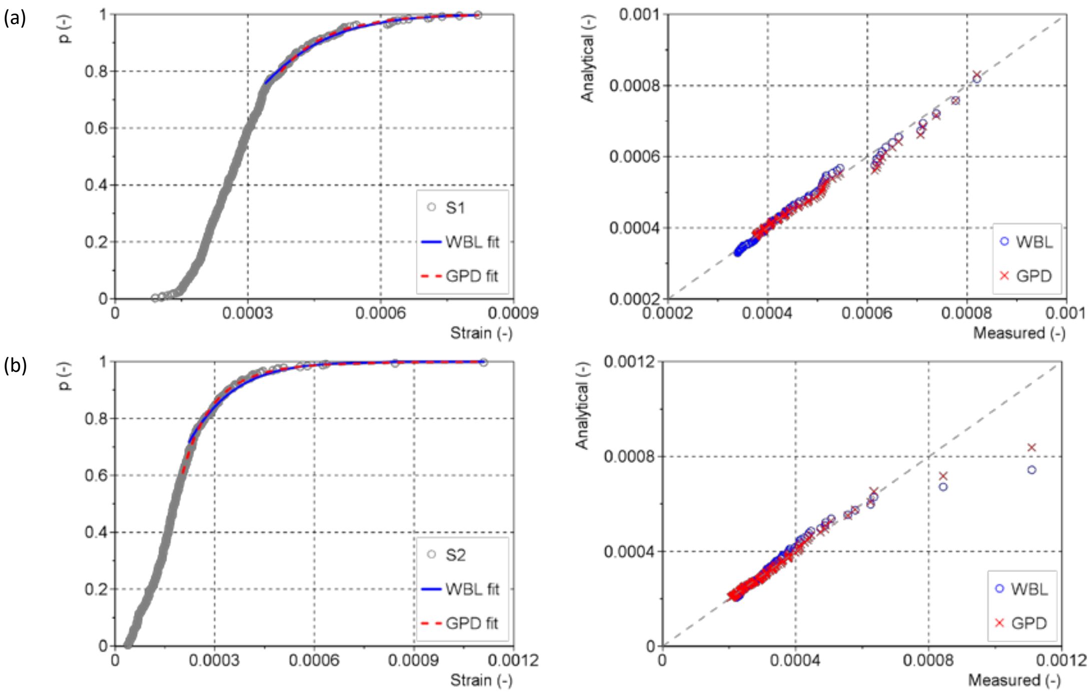

Figure 19 - Cumulative distributions of strain peaks and fitted analytical models and corresponding Quantile-Quantile plots for peak samples S1 (a) and S2 (b), run 2.

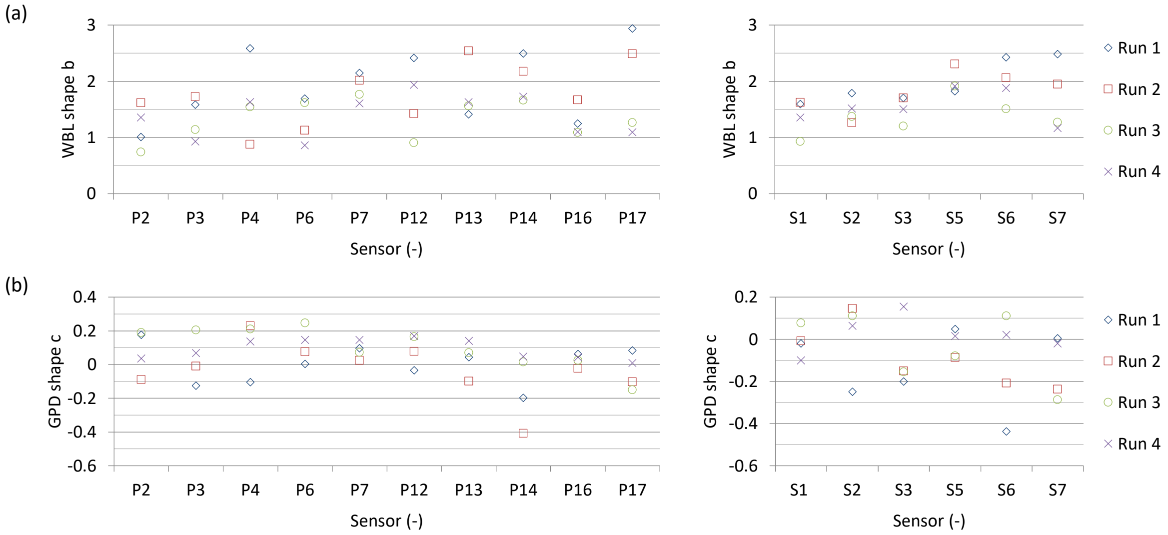

Figure 20 - Weibull (a) and Generalized Pareto (b) shape parameters for the pressure and strain peak samples, runs 1 - 4.

Extreme value estimates are sensitive to the accuracy of the model fit to the data - if a model does not accurately represent the measured data it will most likely not work well when extrapolating for extreme values (Coles 2001). In the present work, the relative goodness of fit of the models is examined using Quantile-Quantile plots and the RMSE statistic. In Quantile-Quantile plots the measured data is plotted against the theoretical quantile values from the fitted model and if the model is a good fit to the data points, they should fall on a straight y = x line. As can be seen from Figures 18 and 19 both the Weibull and Generalized Pareto models fit the data relatively well. In general, the models fail to accurately predict the tail of the distribution; in particular the largest peaks that differ greatly from rest of the peaks in the sample, e.g. the largest three peaks recorded at S2 are 1110 μs, 843 μs and 635 μs, respectively. This is also reflected in the root mean square errors (RMSE), presented in Figure 21 and Tables 15 and 16. The RMSE range from 1.4 to 16.8 % and are generally larger for both pressure and strain distributions from runs 3 and 4. The Weibull and Generalized Pareto errors are comparable for runs

1 – 3, while for run 4 the Generalized Pareto is generally a better fit to both the pressure and strain distributions. From assessment of the Quantile-Quantile plots and RMSE for all peak samples it can be concluded that a RMSE value of less than about 2 percent indicates that the model is an excellent fit to the data, while larger errors typically indicate that the largest peaks are not very well predicted by the statistical models.

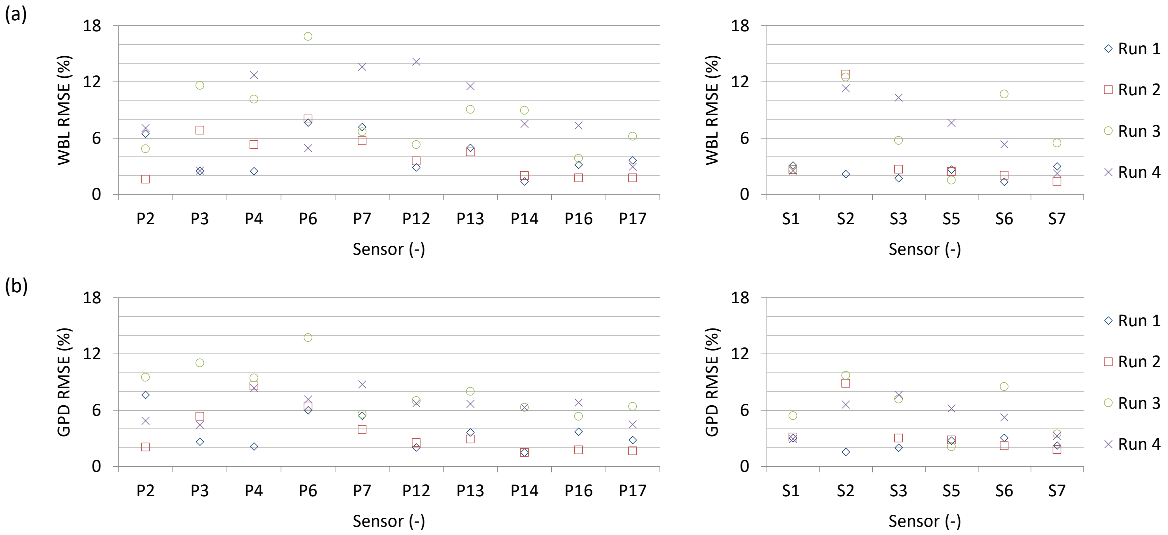

Figure 21 - Normalized root mean square errors (RMSE) (%) for the Weibull and Generalized Pareto models - pressure and strain peaks samples and runs 1 – 4.

In Figure 22 the most probable extreme values and extreme values with 1% probability of being exceeded in a 5 minute period – the duration of the runs - estimated using the Weibull and Generalized Pareto models are presented. As can be seen, the estimated most probable extreme values using the Weibull and Generalized Pareto models (solid bars) agree relatively well. The difference between the two estimates is in most cases less than 15% and the largest difference is 32.6 % for peak sample P12 in run 4. The estimated extreme values with low probability of exceedance however show quite significant differences. This is mainly attributed to the inaccurate modelling of the distribution tail – largest differences are generally observed for the cases with high RMSE.

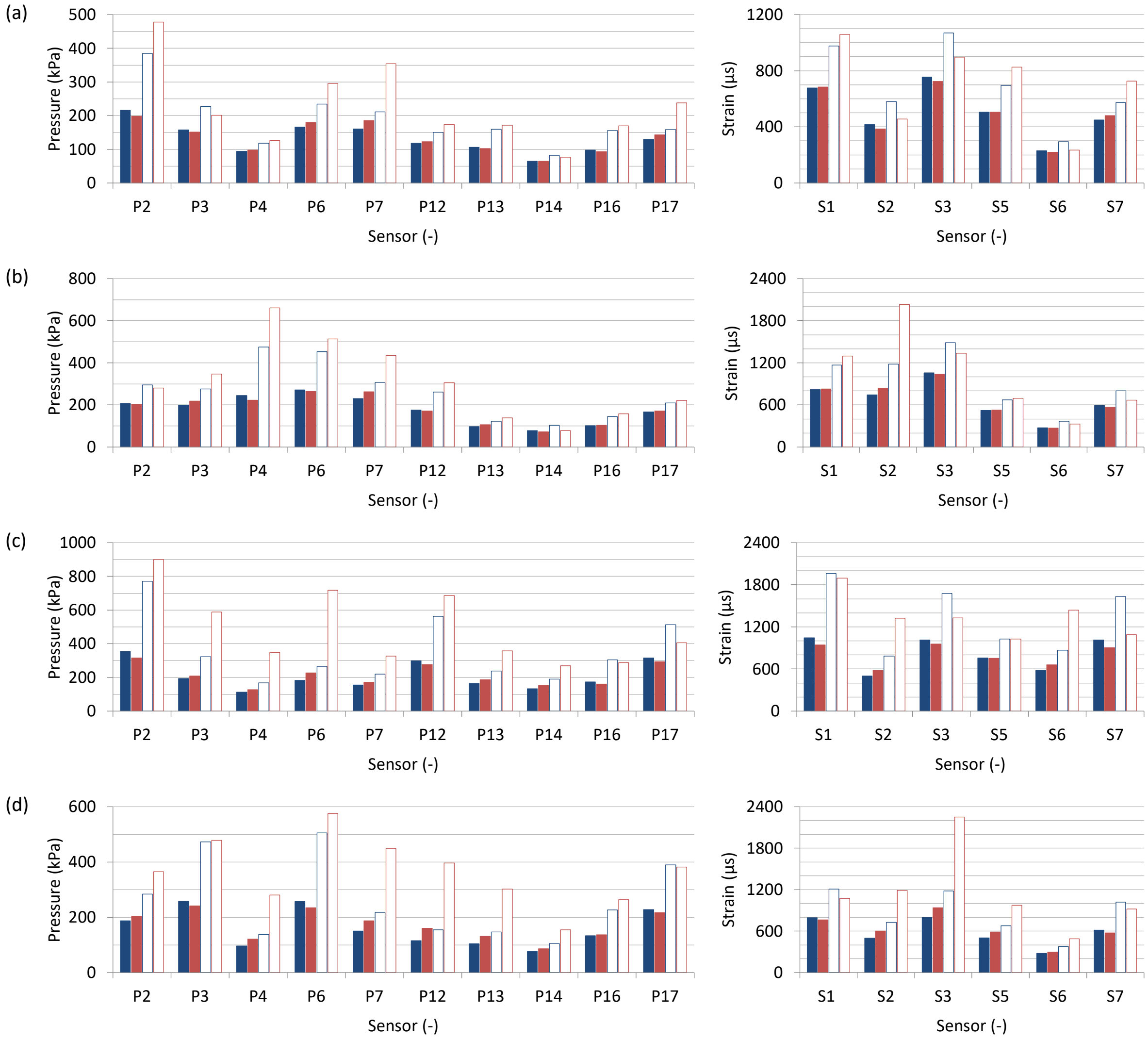

Figure 22 – Estimates of most probable extreme pressures and strains (solid bars) and extreme pressures and strains with 1% probability of exceedance (empty bars) using Weibull (blue) and Generalized Pareto (red) models for runs 1 – 4 (a – d).

5.3. Comparison with design rules of high-speed craft

In this section the pressures measured in the full-scale tests are compared with the predictions based on the rules of two classification societies and the ISO standard for small hull construction (ISO 2008) to assess the suitability of the design loads used in current practice. The classification society rules chosen are the DNV GL rules for classification of high speed and light craft (DNV GL 2015) and Lloyd's Register rules and regulations for the classification of special service craft (Lloyd's Register 2016). The methods and formulas implemented in the these rules and standard are similar and are largely based on the semi-empirical works of Savitsky & Brown (1976) and Allen & Jones (1978). In short, a uniform static design pressure load is calculated for each hull structural component (e.g. plating, stiffeners etc.) for stress analysis and scantling determination. The design pressure load is mainly expressed in terms of the main particulars of the craft (length, beam and displacement), size and longitudinal location of the component being considered and the vertical acceleration at the longitudinal centre of gravity.

Comparisons are made for the pressures measured on the panels where sensors P2 and P3 and sensors P6 and P7 are installed and the corresponding starboard side pressure measurements – see Figures 2 and 15 – which are here referred to as panels A and B respectively. Figure 23 shows the design slamming pressure predictions based on the ISO standard and DNV GL and LR rules for panels A and B and runs 1 – 4. The ISO standard and DNV

GL rules specify maximum limits on the design vertical acceleration of 7g and 6g respectively. In Figure 23, in cases where the predicted design vertical acceleration is less than or equal to the maximum limit, the design slamming pressures are represented by solid columns, whereas in cases where the acceleration is greater than the maximum limit the pressures are represented by stacked columns with the empty portion representing the difference between the prediction and maximum limit. The LR rules do not specify maximum limits. The ISO accelerations are considered to be close to the single amplitude acceleration at the relevant frequency for a certain period of time, whereas the LR accelerations are the average of the 1/100th highest accelerations. The DNV GL rules do not explicitly state the statistical level. The statistical level used to describe the accelerations (e.g. average of 1/100th etc.) is also the resulting statistical level of the design slamming pressures (Koelbel 1995). Direct comparisons between the three predictions and between predictions and measurements should therefore be made with care. Furthermore, these methods are intended for the lifetime of the craft rather than particular runs. As can be seen, the three methods predict the largest design slamming pressures for run 2 – highest speed - and smallest for run 4 - slowest speed. It can also be observed that the three methods predict very similar design pressure for panels A and B for all runs which is to be expected as the geometrical characteristics of these two panels are not that different.

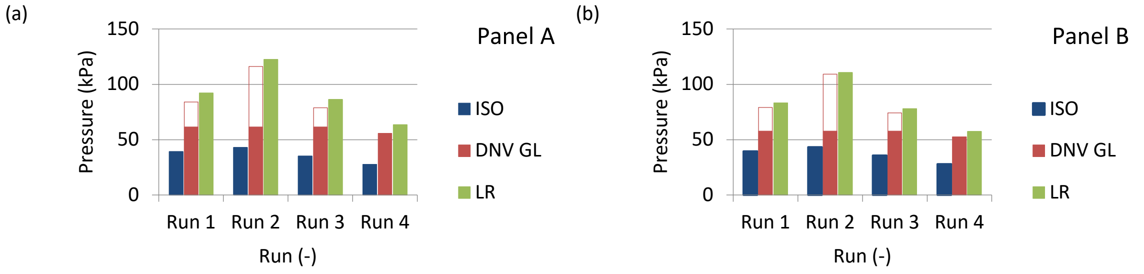

Figure 23 - ISO, DNV GL and LR pressure predictions for panels A (a) and B (b), runs 1 - 4.

The design slamming pressures represent average uniform pressures over the area of the structural component being considered. The area of panels A and B is 0.262 m^2 and 0.253 m^2, respectively. On the other hand, the statistical quantities derived from the measured data, i.e., the averages of the largest 1/3rd and 1/10th peak values, most probable extreme values and so on, are based on maximum pressures measured by the sensors with a diaphragm area of 23.8 mm^2. To compare the measured and predicted pressures, the measured values are scaled using the pressure reduction coefficient of Allen & Jones (1978). This coefficient relates the maximum pressure P_M acting on the area of the structural component considered A_D to the average pressure P_D on the same area, and decreases with increasing area of the structural member (presented as a fraction of the reference area A_R) as shown in figure 17 of Allen & Jones (1978). The reference area is defined as that approximate amount of the hull bottom involved in a major impact and was introduced to enable direct comparisons of data from different hulls. The reference area of the C-Target 9 is 4.45 m^2 and the ratio A_D/A_R is approximately 0.058 for both panels A and B. Thus, from figure 17 of Allen & Jones (1978), the pressure reduction coefficient $K_D = P_D/P_M$ is 0.32.

Figure 24 compares the pressures measured on panels A (P2, P3, P12 and P13) and B (P6, P7, P16 and P17) in runs 1 – 4 with the design slamming pressures based on the formulas given in the ISO standard and DNV GL and LR rules. The experimental results include the averages of the largest 1/10th peaks values, maximum values, and the Weibull and generalized Pareto most probable extreme values and are multiplied by the pressure reduction coefficient (= 0.32). The predicted values presented in Figure 24 take into account the maximum limit on the design vertical acceleration in order to represent the design slamming pressure that would be used by the designer. As can be seen, the ISO standard and DNV GL rules predict pressures that are significantly lower than the measured maximum pressures and estimated most probable extremes, for both panels and all runs but more particularly runs 2 – 4. The differences are larger for the ISO pressures. The LR rules predict pressures that are higher than or comparable to the measured maximum pressures and estimated most probable extremes for runs 1 and 2 – high forward speed – while for runs 3 and 4 the predictions are lower than the measured data but greater than the ISO and DNV GL pressures. The large differences between the LR pressures and ISO and DNV GL pressures are mainly due to the fact that the LR rules do not impose any maximum limits on the design vertical accelerations.

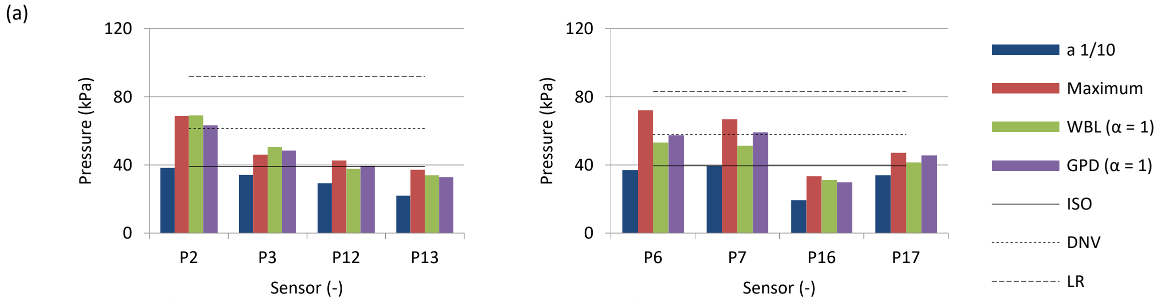

Run 1 - Panel A
Run 1 - Panel B

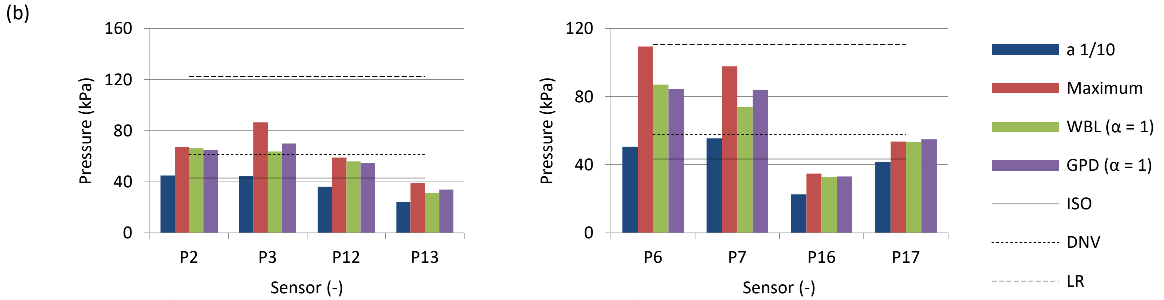

Run 2 - Panel A
Run 2 - Panel B

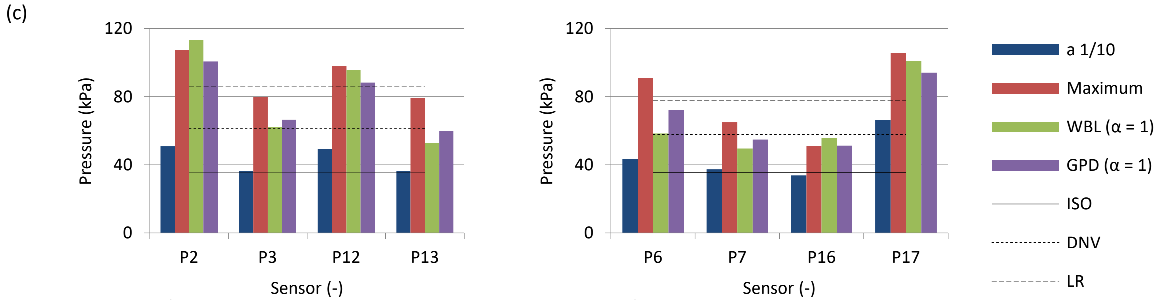

Run 3 - Panel A
Run 3 - Panel B

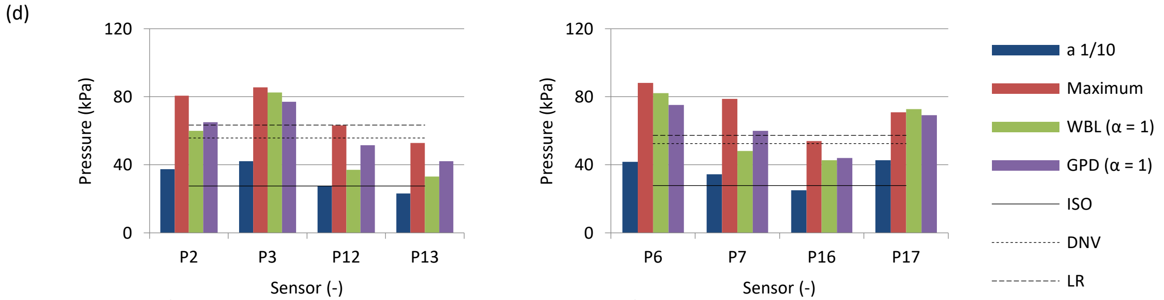

Run 4 - Panel A
Run 4 - Panel B

Figure 24 – Comparison of measured pressures with ISO, DNV GL and LR pressure predictions for panels A (1st column) and B (2nd column), runs 1 – 4.

The minimum required thickness of panels A and B by the ISO standard and DNV GL and LR rules for runs 1 – 4 are given in Table 4. The minimum required thickness to withstand the design loads is determined using standard strength formulae where satisfactory strength level is represented by allowable stress. The material is Aluminium 5083-O and the allowable stress is 113, 120 and 125 N/mm^2 respectively. The scantling requirements show similar trends, namely that the ISO standard and LR rules are the least and most stringent, respectively, and the DNV GL rules lie in between.

Table 4 - Minimum required thickness of panels A and B, runs 1 - 4.

	Panel A, mm			Panel B, mm		
	ISO	DNV GL	LR	ISO	DNV GL	LR
Run 1	4.5	5.3	7.1	4.3	5.0	6.5
Run 2	4.7	5.3	8.2	4.6	5.0	7.5
Run 3	4.2	5.3	6.9	4.1	5.0	6.3
Run 4	3.8	5.1	5.9	3.7	4.8	5.4

6. Conclusions

Full-scale trials on a 9.6m high-speed planing craft in waves have been performed to investigate the characteristics of slamming impacts and related rigid body and structural response. An extensive set of experimental data consisting of accelerations, pressure and strain at various locations across the hull bottom surface and global hull deflections in different sea conditions and at different forward speeds and headings was recorded. In the present study, acceleration pressure and strain measurements made in head seas for varying speeds and sea conditions are considered with the aim to illustrate the data processing procedure and also present and discuss characteristic results. The following conclusions can be drawn from this study:

- The raw acceleration signals contain unwanted high frequency noise that is concluded to be due to structural and engine vibrations. Fast Fourier Transform (FFT) and low pass filtering are used to calculate the energy content of the signal and remove the high-frequency noise, respectively. It is found that a cut-off frequency of 30Hz effectively removes the high-frequency noise without significantly influencing the signal characteristics, particularly the rapid increase in acceleration with impact.
- Methods for removing the trends from strain signals and identifying the peaks in the pressure and strain signals are developed and successfully applied. The peak identification method is found to accurately identify the peaks in all signals based on visual examination, considering that the duration of the interval between impacts and the duration of impacts varies within each signal and also between signals.
- The stochastic and nonlinear behaviour of a planing craft travelling at high speed in waves is clearly illustrated in the measurements where each hull-water impact is different. In general, the impacts are characterised by short rise time and large peaks of short duration, with the magnitude of pressure and strain decreasing with increasing distance from the keel and forward. Strong correlation between the pressure and strain signals is also observed. The impacts are fairly symmetric in terms of the number of peaks recorded on the port and starboard sides; however, the averages of the largest 1/3rd and 1/10th peak values show some differences with the port side measurements being generally larger. The statistical averages also show that larger pressures and strains were measured at high speed in moderate seas rather than at moderate speed in rough seas.
- The statistical analysis showed that pressure and strain peaks on different levels were found to belong to different statistical distributions, with large magnitude peaks which are most likely to be due to extreme slamming impacts being more nonlinear. This observation justifies the use of a threshold in fitting the Weibull model to better model the largest peaks. Overall, the statistical models were found to fit the data well except in the tail of the distribution, particularly for samples that contain outliers. The methods used in the present work to estimate the model parameters and select the threshold (least square method for the Weibull and method of moments and shape parameter stability plots for the GPD) have been shown to perform well in statistical analyses of wave loads on large ships, however for full-scale measurements of slamming loads on high-speed craft, where samples can contain outliers

and the sample sizes are generally small, more robust methods may be needed (see for instance de Zea Bermudez & Kotz (2010) for a review of robust methods).

- The pressure predictions based on the ISO standard and DNV GL and LR rules generally did not match the measured data. In particular, the ISO standard and DNV rules predict pressures that are significantly lower than the measured values, while the LR rules predict pressures that are larger or comparable to the measured data for high forward speed runs and lower than the measured data for moderate speed runs. The present comparative study is quite limited regarding the craft geometry, sea and run conditions, and structural components studied. However, it is quite clear that more accurate prediction methods are required for designing safe and efficient modern high-speed craft structures.

Acknowledgements

This research was financially supported by the Defence, Science & Technology Laboratory (contract DSTLX-1000081794) and the Engineering and Physical Sciences Research Council UK (grant EP/L505067/1). The assistance of ASV global in instrumenting the boat and conducting the sea trials is also gratefully acknowledged.

Appendix A

Table 5 - Number of pressure peaks identified in signals P1 – P20, runs 1 - 4.

Run	P1 (P11)	P2 (P12)	P3 (P13)	P4 (P14)	P5 (P15)	P6 (P16)	P7 (P17)	P8 (P18)	P9 (P19)	P10 (P20)
1	67 (66)	343 (341)	370 (373)	321 (273)	97 (144)	329 (332)	303 (301)	141 (140)	117 (109)	24 (59)
2	113 (98)	390 (389)	420 (430)	357 (324)	133 (214)	365 (366)	370 (362)	194 (149)	124 (120)	39 (110)
3	197 (196)	374 (373)	344 (350)	243 (261)	122 (149)	234 (249)	230 (239)	167 (139)	94 (90)	68 (133)
4	51 (52)	447 (444)	433 (442)	351 (343)	157 (178)	334 (345)	298 (308)	204 (281)	122 (120)	76 (104)

Table 6 - Number of strain peaks identified in signals S1 – S8, runs 1 - 4.

Run	S1 (S5)	S2 (S6)	S3 (S7)	S4 (S8)
1	336 (335)	280 (241)	301 (285)	94 (85)
2	365 (358)	323 (258)	361 (361)	114 (100)
3	331 (329)	229 (235)	241 (252)	95 (101)
4	422 (410)	326 (300)	315 (309)	120 (117)

Table 7 - Average of the largest 1/3rd pressure peaks (kPa) for P1 – P20, runs 1 - 4.

Run	P1 (P11)	P2 (P12)	P3 (P13)	P4 (P14)	P5 (P15)	P6 (P16)	P7 (P17)	P8 (P18)	P9 (P19)	P10 (P20)
1	29.7 (32.4)	90.8 (75.4)	81.2 (54.4)	62.1 (42.5)	47.8 (5.9)	88.1 (46.3)	96.7 (89.7)	52.1 (29.4)	96.7 (66.5)	30.5 (10)
2	44 (31.5)	107.9 (90.7)	104.4 (62.7)	91.3 (47.8)	64.7 (9)	115 (54.6)	133.5 (107.2)	74.8 (35)	113.8 (82.8)	44.6 (11.3)
3	64.4 (107.1)	101.8 (111.2)	79.3 (82.8)	58.3 (71.3)	49.6 (42.5)	97.4 (74.5)	87.1 (144.3)	48.5 (55.6)	100.1 (107)	40.1 (27.4)
4	96.6 (57.4)	83.3 (64)	89.5 (52.2)	49.7 (40.5)	59.8 (33.3)	88.1 (52)	78.2 (93.1)	50.6 (27.4)	86.6 (66.2)	37.8 (17.5)

Table 8 - Average of the largest 1/3rd strain peaks (μs) for S1 – S8, runs 1 – 4.

Run	S1 (S5)	S2 (S6)	S3 (S7)	S4 (S8)
1	352.5 (292)	232.2 (150.3)	411.3 (294.3)	211.9 (82.4)
2	425.3 (327.7)	325.9 (166)	562 (342.6)	347.4 (116.4)
3	396.4 (431.3)	242.8 (298.7)	445.5 (462.6)	235.9 (248.3)
4	359.6 (280)	245.2 (157)	398.2 (271.5)	267.7 (145.7)

Table 9 - Average of largest 1/10th pressure peaks (kPa) for P1 – P20, runs 1 - 4.

Run	P1 (P11)	P2 (P12)	P3 (P13)	P4 (P14)	P5 (P15)	P6 (P16)	P7 (P17)	P8 (P18)	P9 (P19)	P10 (P20)
1	38.5 (39.4)	119.8 (91.6)	106.8 (68.4)	75.1 (51.8)	60.8 (9)	115.7 (60.6)	123.5 (106.4)	67.2 (40.3)	131.2 (82.7)	44.4 (16.9)
2	68 (35.1)	140.4 (113)	139.8 (76.4)	124.3 (60)	95.3 (17)	158.4 (70.6)	173.1 (130.8)	105.2 (45.5)	158.6 (106.3)	74.9 (21.2)
3	91.4 (156.6)	158.7 (154.2)	113.8 (113.6)	80.3 (97.6)	78.2 (64.7)	135.4 (105.7)	117 (207)	77.9 (79.1)	135 (147.1)	71.3 (67.9)
4	137.2 (74.4)	116.9 (86.6)	131.9 (72.3)	69 (54.4)	83.4 (54.1)	130.4 (78.3)	107.8 (133.4)	72.5 (42.2)	114.8 (96.9)	60.7 (30.8)

Table 10 - Average of largest 1/10th strain peaks (μs) for S1 – S8, runs 1 – 4.

Run	S1 (S5)	S2 (S6)	S3 (S7)	S4 (S8)
1	460.5 (359.7)	300.7 (182.2)	537.5 (359.8)	338.2 (127.2)
2	561.3 (399.3)	464.9 (211.5)	738.9 (431.7)	583.8 (190.2)
3	555.8 (550.4)	353.1 (416)	640.8 (660)	348.9 (346.7)
4	499.3 (371.4)	348.3 (201.8)	550.1 (372.7)	365.5 (197.8)

Table 11 - Weibull distribution shape (-) and scale (kPa) parameters for the pressure peaks samples, runs 1 - 4.

Run	Parameter	P2	P3	P4	P6	P7	P12	P13	P14	P16	P17
1	Shape, b	1.01	1.58	2.58	1.69	2.14	2.41	1.41	2.49	1.25	2.94
	Scale, a	37.3	51.3	47.9	58.6	71.0	56.9	30.2	32.4	23.8	71.6
2	Shape, b	1.62	1.72	0.88	1.13	2.01	1.42	2.54	2.18	1.67	2.49
	Scale, a	68.6	70.2	32.5	56.4	95.4	49.9	48.2	35.0	35.4	81.8
3	Shape, b	0.74	1.14	1.54	1.62	1.76	0.91	1.56	1.66	1.09	1.26
	Scale, a	31.8	41.1	37.2	64.0	59.2	42.1	53.1	47.2	36.2	82.1
4	Shape, b	1.36	0.93	1.63	0.86	1.61	1.94	1.63	1.73	1.10	1.10
	Scale, a	49.3	37.1	32.6	33.4	51.1	45.5	34.2	27.2	26.8	46.2

Table 12 - Weibull distribution shape (-) and scale (μs) parameters for the strain peaks samples, runs 1 - 4.

Run	Parameter	S1	S2	S3	S5	S6	S7
1	Shape, b	1.59	1.79	1.70	1.82	2.42	2.48
	Scale, a	224.1	157.8	271.7	192.3	113.6	224.3
2	Shape, b	1.62	1.26	1.70	2.31	2.06	1.94
	Scale, a	273.9	185.0	374.5	242.3	119.7	238.6
3	Shape, b	0.93	1.37	1.20	1.91	1.51	1.27
	Scale, a	156.7	146.1	246.2	301.4	188.7	264.2
4	Shape, b	1.36	1.51	1.51	1.91	1.88	1.17
	Scale, a	210.8	155.3	250.5	196.7	109.0	137.5

Table 13 – Generalized Pareto shape (-) and scale (kPa) parameters for the pressure peaks samples, runs 1 - 4.

Run	Parameter	P2	P3	P4	P6	P7	P12	P13	P14	P16	P17
1	Shape, c	0.18	-0.12	-0.10	0.00	0.10	-0.03	0.04	-0.20	0.06	0.08
	Scale, λ	19.6	24.4	12.6	24.4	19.5	13.8	10.8	9.1	10.9	12.1
2	Shape, c	-0.09	-0.01	0.23	0.07	0.02	0.08	-0.10	-0.41	-0.02	-0.10
	Scale, λ	30.3	29.9	20.0	30.4	32.0	16.1	15.3	14.9	13.8	21.6
3	Shape, c	0.19	0.21	0.21	0.25	0.07	0.17	0.07	0.01	0.02	-0.15
	Scale, λ	33.3	22.7	12.6	22.2	21.5	28.5	22.9	23.0	24.0	60.1
4	Shape, c	0.04	0.07	0.14	0.15	0.15	0.17	0.14	0.05	0.04	0.01
	Scale, λ	26.6	30.8	13.0	24.8	19.9	13.9	13.6	10.9	20.7	33.5

Table 14 – Generalized Pareto shape (-) and scale (μs) parameters for the strain peaks samples, runs 1 - 4.

Run	Parameter	S1	S2	S3	S5	S6	S7
1	Shape, c	-0.02	-0.25	-0.20	0.05	-0.44	0.00
	Scale, λ	92.9	70.1	131.7	51.1	68.7	51.5
2	Shape, c	-0.01	0.15	-0.15	-0.09	-0.21	-0.24
	Scale, λ	107.8	90.1	171.9	63.5	45.2	99.1
3	Shape, c	0.08	0.11	-0.16	-0.08	0.11	-0.29
	Scale, λ	120.4	80.6	206.9	100.3	84.1	225.3
4	Shape, c	-0.10	0.06	0.16	0.02	0.02	-0.02
	Scale, λ	129.4	84.2	102.6	75.6	36.3	87.6

Table 15 – Normalized root mean square errors (%) for the Weibull and Generalized Pareto models, pressure peaks samples, runs 1 – 4.

Run	Model	P2	P3	P4	P6	P7	P12	P13	P14	P16	P17
1	WBL	6.5	2.5	2.5	7.7	7.2	2.9	5.0	1.4	3.1	3.6
	GPD	7.6	2.7	2.1	6.0	5.4	2.0	3.6	1.5	3.7	2.8
2	WBL	1.6	6.9	5.3	8.1	5.7	3.6	4.5	2.0	1.8	1.8
	GPD	2.1	5.3	8.6	6.4	3.9	2.6	2.9	1.5	1.8	1.7
3	WBL	4.9	11.6	10.2	16.8	6.7	5.3	9.1	9.0	3.8	6.2
	GPD	9.5	11.1	9.5	13.8	5.6	7.0	8.0	6.3	5.3	6.4
4	WBL	7.1	2.6	12.7	4.9	13.6	14.2	11.6	7.5	7.4	3.0
	GPD	4.9	4.5	8.3	7.2	8.8	6.7	6.7	6.3	6.8	4.5

Table 16 - Normalized root mean square errors (%) for the Weibull and Generalized Pareto models, strain peaks samples, runs 1 – 4.

Run	Model	S1	S2	S3	S5	S6	S7
1	WBL	3.1	2.2	1.7	2.6	1.4	3.0
	GPD	3.0	1.5	2.0	2.8	3.1	2.2
2	WBL	2.7	12.8	2.7	2.5	2.0	1.4
	GPD	3.1	8.9	3.0	2.8	2.2	1.8
3	WBL	2.7	12.5	5.8	1.5	10.7	5.5
	GPD	5.4	9.7	7.2	2.1	8.5	3.5
4	WBL	2.5	11.3	10.3	7.6	5.3	2.2
	GPD	3.0	6.6	7.6	6.2	5.2	3.3

References

Akers, R.H., 1999. Dynamic Analysis of Planing Hulls in the Vertical Plane. In *Proceedings of the Society of Naval Architects and Marine Engineers, New England Section*.

Allen, D.P., Taunton, D.J. & Allen, R., 2008. A study of shock impacts and vibration dose values onboard high-speed marine craft. *Transactions of the Royal Institution of Naval Architects Part A: International Journal of Maritime Engineering*, 150(3), pp.1–10.

Allen, R.G. & Jones, J.R., 1978. A simplified method for determining structural design limit pressures on high performance marine vehicles. In *AIAA/SNAME Advance Marine Vehicles Conference*. San Diego, California.

Allen, T. & Battley, M., 2015. Quantification of hydroelasticity in water impacts of flexible composite hull panels. *Ocean Engineering*, 100, pp.117–125.

ASV, 2017. C-Target 9 Product Information. Available at: http://asvglobal.com/product/c-target-9/ [Accessed January 6, 2017].

Begovic, E., Bertorello, C. & Pennino, S., 2014. Experimental seakeeping assessment of a warped planing hull model series. *Ocean Engineering*, 83, pp.1–15.

Begovic, E., Bertorello, C., Pennino, S., Piscopo, V. & Scamardella, A., 2016. Statistical analysis of planing hull motions and accelerations in irregular head sea. *Ocean Engineering*, 112, pp.253–264.

Blake, J.I.R. & Wilson, P.A., 2001. An analysis of planing craft vertical dynamics in calm water and in waves. In *6th International Conference on Fast Sea Transportation*. Southampton, UK, pp. 77–89.

Coles, S., 2001. *An Introduction to Statistical Modeling of Extreme Values*, London: Springer.

DNV, 1997. *Tentative Rules for Certification and Classification of Boats*, Høvik, Norway.

DNV GL, 2015. Part 3 Structures, equipment. In *DNV GL rules for classification: High speed and light craft*.

Dupuis, D.J. & Tsao, M., 1998. A hybrid estimator for generalized pareto and extreme-value distributions. *Communications in Statistics - Theory and Methods*, 27(4), pp.925–941.

Faltinsen, O.M., Landrini, M. & Greco, M., 2004. Slamming in marine applications. *Journal of Engineering Mathematics*, 48(3/4), pp.187–217.

Fridsma, G., 1971. *A Systematic Study of the Rough-Water Performance of Planing Boats (Irregular Waves - Part II)*, New Jersey.

Garme, K., 2005. Improved Time Domain Simulation of Planing Hulls in Waves by Correction of the Near-Transom Lift. *International Shipbuilding Progress*, 52(3), pp.201–230.

Garme, K. & Rosén, A., 2003. Time-Domain Simulations and Full-Scale Trials on Planing Craft in Waves. *International Shipbuilding Progress*, 50(3), pp.177–208.

Graczyk, M. & Moan, T., 2008. A probabilistic assessment of design sloshing pressure time histories in LNG tanks. *Ocean Engineering*, 35(8–9), pp.834–855.

ISO, 2008. Part 5: Design pressures for monohulls, design stresses, scantlings determination (ISO 12215-5:2008). In *Small craft - Hull construction and scantlings*.

Jacobi, G., Thomas, G., Davis, M.R. & Davidson, G., 2014. An insight into the slamming behaviour of large high-speed catamarans through full-scale measurements. *Journal of Marine Science and Technology (Japan)*, 19(1), pp.15–32.

Judge, C.Q., Judge, J.A. & Ikeda, C., 2015. Impact Pressures on the Bottom of a Prismatic Planing Hull During Water Impact. In *13th International Conference on Fast Sea Transportation FAST 2015*.

von Karman, T., 1929. The impact on seaplane floats during landing.

Keuning, J.A., 1994. *Nonlinear Behaviour of Fast Monohulls in Head Waves*. Delft University of Technology.

Koelbel, J.G., 1995. Comments on the Structural Design of High Speed Craft. *Marine Technology*, 32(2), pp.77–

100.

Korobkin, A., 2004. Analytical models of water impact. *European Journal of Applied Mathematics*, 15(6), pp.821–838.

Lewis, S.G., Hudson, D.A., Turnock, S.R. & Taunton, D.J., 2010. Impact of a Free-Falling Wedge with Water: Synchronized Visualization, Pressure and Acceleration Measurements. *Fluid Dynamics Research*, 42, p.30.

Lloyd's Register, 2016. Part 5 Design and Load Criteria. In *Rules and Regulations for Classification of Special Service Craft*.

McCue, L., 2012. Statistics and Design Implications of Extreme Peak Vertical Accelerations from Slamming of Small Craft. *Journal of Ship Production and Design*, 28(3), pp.112–127.

Mørch, H.J.B. & Hermundstad, O.A., 2005. Planing Craft in Waves - Full-Scale Measurements. In *8th International conference on Fast Sea Transportation FAST 2005*. St. Petersburg, Russia.

National Instruments, 2017. DIAdem. Available at: http://www.ni.com/diadem/ [Accessed June 17, 2017].

Ochi, M.K., 1981. Principles of extreme value statistics and their application SNAME, ed. *Extreme Loads Response Symposium*, pp.15–30.

Pickands, J., 1975. Statistical inference using extreme order statistics. *The Annals of Statistics*, 3(1), pp.119–131.

Piro, D.J. & Maki, K.J., 2013. Hydroelastic analysis of bodies that enter and exit water. *Journal of Fluids and Structures*, 37, pp.134–150.

Razola, M., Olausson, K., Garme, K. & Rosén, A., 2016. On high-speed craft acceleration statistics. *Ocean Engineering*, 114, pp.115–133.

Riley, M.R., Coats, T.W., Haupt, K. & Jacobson, D., 2013. Ride Severity Index: A Simplified Approach for Comparing Peak Acceleration Responses of High-Speed Craft. *Journal of Ship Production and Design*, 29(1), pp.25–35.

Riley, M.R., Coats, T.W. & Murphy, H., 2014. *Acceleration Response Mode Decomposition for Quantifying Wave Impact Load in High-Speed Planing Craft*, West Bethesda.

Rosén, A. & Garme, K., 2004. Model Experiment Addressing The Impact Pressure Distribution On Planing Craft In Waves. *International Journal of Small Craft Technology*, 146(B1), p.15.

Savitsky, D., 2016. Direct Measure of Rigid Body Accelerations for Wave Impact of a Planing Hull. *Journal of Ship Production and Design*, 32(2), pp.1–10.

Savitsky, D. & Brown, P.W., 1976. Procedures for hydrodynamic evaluation of planing hulls in smooth and rough water. *Marine Technology*, 13(4), pp.381–400.

Stenius, I., Rosén, A. & Kuttenkeuler, J., 2011. Hydroelastic interaction in panel-water impacts of high-speed craft. *Ocean Engineering*, 38(2–3), pp.371–381.

Taunton, D.J., Hudson, D.A. & Shenoi, R.A., 2011. Characteristics of a series of high speed hard chine planing hulls - part II: Performance in waves. *International Journal of Small Craft Technology*, 153(B1).

Temarel, P., Bai, W., Bruns, A., Derbanne, Q., Dessi, D., Dhavalikar, S., Fonseca, N., Fukasawa, T., Gu, X., Nestegard, A., Papanikolaou, A., Parunov, J., Song, K.H. & Wang, S., 2016. Prediction of wave-induced loads on ships: Progress and challenges. *Ocean Engineering*, 119, pp.274–308.

Tveitnes, T., Fairlie-Clarke, A.C. & Varyani, K., 2008. An experimental investigation into the constant velocity water entry of wedge-shaped sections. *Ocean Engineering*, 35(14–15), pp.1463–1478.

VanDerwerken, D. & Judge, C., 2017. Statistical analysis of vertical accelerations of planing craft: Common pitfalls and how to avoid them. *Ocean Engineering*, 139(October 2016), pp.265–274. Available at: http://dx.doi.org/10.1016/j.oceaneng.2017.05.004.

Wagner, H., 1932. Phenomena associated with impacts and sliding on liquid surfaces. *Z. Angew. Math. Mech*, 12(4), pp.193–215.

Wang, L. & Moan, T., 2004. Probabilistic analysis of nonlinear wave loads on ships using weibull, generalized gamma, and pareto distributions. *Journal of Ship Research*, 48(3), pp.202–217.

Wu, M. & Moan, T., 2006. Statistical analysis of wave-induced extreme nonlinear load effects using time-domain simulations. *Applied Ocean Research*, 28(6), pp.386–397.

Zarnick, E.E., 1979. *A non-linear mathemathical model of motions of a planing boat in irregular waves*, Bethesda, Maryland.

de Zea Bermudez, P. & Kotz, S., 2010. Parameter estimation of the generalized Pareto distribution-Part II. *Journal of Statistical Planning and Inference*, 140(6), pp.1374–1388.

Zhao, R., Faltinsen, O.M. & Aarsnes, J. V, 1996. Water Entry of Arbitrary Two Dimensional Section with and without Flow Separation. In *21st Symposium on Naval Hydrodynamics*. pp. 408–423.